The fate of accessory minerals and key trace elements during anatexis and magma extraction

Martin Schwindinger*[1], Roberto F. Weinberg[1] and Richard W. White[2]

[1]School of Earth, Atmosphere and Environment, Monash University, Clayton, VIC 3800, Australia

[2]School of Earth and Environmental Sciences, The University of St Andrews, St Andrews, United Kingdom

*Corresponding Author Details:

Email: martin.schwindinger@gmail.com

ABSTRACT

Granite genesis and crustal evolution are closely associated with partial melting in the lower or middle crust and extraction of granite magmas to upper levels. This is generally thought to be the leading mechanism by which the upper continental crust became enriched in incompatible components such as the heat-producing elements U and Th through time. However, field evidence from anatectic terrains, the source rocks of granite magmas, raises doubt about the efficiency of this process. Leucosomes and associated leucogranites, representative of melts in such terrains, are often depleted in U, Th and REE compared to their source and therefore unable to enrich the upper crust in these elements. This paper demonstrates using anatectic turbidites exposed on Kangaroo Island that accessory minerals, the main host of U, Th and REE, become preferentially concentrated in the melanosomes, effectively removing these elements from the melt. Whole rock geochemistry and detailed petrography suggests that (a) peraluminous melts dissolve only small fractions of monazite and xenotime, because efficient apatite dissolution saturates melt early in phosphorous; and (b) local melt–host reaction emerging from melt migration may cause substantial melt to crystallize in the magma extraction channelways in or close to the magma source region. Crystallization causes oversaturation of the magma triggering the crystallization and capture of accessory minerals in the growing biotite-rich selvedge rather than in the melt channel itself. Crystallization of accessory minerals away from the leucosomes explains the apparent under-saturation of elements hosted by these accessory minerals in the leucosome. While intense reworking of thick piles of turbidites, common in accretionary orogens, reflect important processes of crustal formation, the fate of accessory phases and the key elements they control, such as the heat producing elements U and Th, is strongly dependent on the interaction between melt and surrounding solids during segregation and extraction.

Keywords: REE, accessory minerals, migmatite, granite, anatexis,

INTRODUCTION

Thick turbidite sequences form vast volumes of material that are added to the margin of accretionary orogens where they are strongly reworked and ultimately become part of crystalline continents (Cawood et al., 2009; Weinberg et al., 2018). The latter takes place via their partial melting under amphibolite to granulite facies conditions (e.g. Johnson et al., 2008), followed by extraction of granite magmas. This process is interpreted to be a leading mechanism by which the continental crust differentiates into an upper crust enriched in incompatible elements, and a residual, depleted lower crust (Brown and Rushmer, 2006; Sawyer et al., 2011).

This model has shortcomings revealed when the sources of granitic magmas, the exposed anatectic sections of the middle to lower crust, are directly investigated (Aranovich et al., 2014). Preserved leucosomes and associated leucogranites within migmatite terranes commonly differ in their major and trace elements from average composition of upper crustal granites or melt inclusions (Bartoli et al., 2016; Clemens and Stevens, 2012). Provided little incorporation of restitic minerals into the melt, small-scale leucosomes as well as many granitic bodies (Sawyer, 1991; Watt et al., 1996; Wolfram et al., 2018) tend to be impoverished in the important heat producing elements such as U and Th and trace elements such as Y, Zr and REE (except Eu), compared to their direct source. This raises questions about the role of anatexis alone as an effective mechanism to transfer these elements from deep crustal sources to the upper crust (Alessio et al., 2018; Yakymchuk and Brown, 2019). While this might be expected during low temperature melting because of the general low solubility of the accessory minerals in the melt, which host the majority of U, Th and REE (Bea, 1996b; Montel, 1993; Watson and Harrison, 1983), the same phenomena is observed

across a range of crustal temperatures and melting reactions (Bea et al., 2007; Watt et al., 1996; Wolfram et al., 2018). Explanations for this behaviour generally agree that it relates to processes occurring during melt generation and early melt migration stages within the source terrain. They include low solubility of accessory minerals in certain magma compositions (Bea et al., 1992; Spear and Pyle, 2002; Wolf and London, 1994), accessory mineral–melt disequilibrium by melt extraction outpacing equilibrium between melt and solids (Bea, 1996a; Clemens and Stevens, 2016; Sawyer, 1991; Watt et al., 1996), or the inclusion of accessory minerals in stable major minerals, impeding their dissolution (Watson et al., 1989).

Besides, the general perception that the lower crust has lower concentrations of heat producing elements (HPE) is still under debate. Roots of volcanic arcs, comprising mafic igneous rocks may indeed be considerably poorer in HPE than the felsic upper crust. However, it has been demonstrated by Alessio et al. (2018), that metapelitic residual granulite-facies lithologies have not been depleted in HPE by partial melting and melt loss. In such environments, there are other processes that could potentially enrich the magma leaving the lower crust, such as the breakdown of residual rocks into the magma or melting of protolith rich in radiogenic elements, such as the ones that produced the granites of Central Iberia (Bea, 2012).

The *in source* processes described are also required to explain a common feature of migmatites: the existence of tonalitic leucosomes derived from K-rich sources. Traditionally, these have been interpreted as felsic cumulates, formed by *in source* crystallization of plagioclase and quartz during melt extraction at declining temperatures (Kriegsman and Hensen, 1998; Sawyer, 1987, 2008). Alternative interpretations emphasize diffusional interaction between melt and source, that evolve with temperature and pressure changes (White and Powell, 2010) or simply as a result of melt migration, even before metamorphic peak temperatures are reached (Nicoli et al., 2017; Taylor et al., 2014). Notably, equilibration

via diffusion of mobile components, such as H_2O, K_2O and Na_2O, have been proposed to be most effective in modifying the proportion of quartz, plagioclase and K-feldspar in leucosomes (Acosta-Vigil et al., 2012; White and Powell, 2010). However, the impact of melt–host interaction and the crystallization of these rock-forming minerals on accessory minerals has not yet been considered.

During anatexis, melt tends to segregate away from the solids forming the typical structure of migmatites: melt segregations form leucosomes, leaving behind a residual rock characterized by the partial or total loss of the melt fraction. Melanosomes are dark-coloured parts of the residuum and are enriched in mafic minerals, typically biotite but may contain also peritectic phases such as cordierite or garnet (Sawyer, 2008). They often border leucosome lenses and layers and form as a result of either significant melt removal, in which case they are residual, or as a result of reaction between melt and surrounding (selvedge, White and Powell, 2010)

Complex melting and crystallisation processes may be particularly well-developed in anatectic terrains characterized by low-temperature melting in the presence of a heterogeneously distributed aqueous fluid phase. Under these conditions melting occurs close to the local solidus, whose exact position is not only controlled by pressure and temperature, but also by H_2O activity (Johannes and Holtz, 1996) and variations in bulk composition of the rock mass. Marginal variations in the equilibrium of the system may dictate: (a) when melt crystallizes in a leucosome, (b) the diffusion of elements between solids and melt in a leucosome, and (c) the saturation and growth of accessory minerals in the melt and immediate surroundings, with direct consequences for the ability of magmas to transport HPE, Zr, Y and REE.

In this contribution, we investigate anatectic metaturbidites from Kangaroo Island to understand how local melt–host interaction evolved as a result of melt migration and its

impact on the composition of leucosomes and the fate of accessory minerals. The paper starts with a description of the main lithological types and their relationships, the background for this study. Following that, the work is divided into two connected parts. The first part describes the fractionation of magma within the source, occurring in a two to five metre long network, where it is possible to track the melt evolution from its extraction to the final intrusive tips, where migration stalls. The second part details the distribution of accessory minerals, which crystallize in response to the evolving nature of the melt as it crystallizes. Both processes, crystallization of the melt and the distribution of accessory minerals, are related to local disequilibrium between magma and surrounding rock in an environment of high diffusivity. We use the term HPE to refer only to U and Th, excluding K. This is because the U-Th budget in crustal rocks is dominated by accessory minerals, while K is controlled by the stability of K-feldspar and micas and evolves independently of the accessory minerals.

GEOLOGICAL SETTING AND LITHOLOGY

Geological Setting

The outcrops of interest are located on the south coast of Kangaroo Island, which is part of the Adelaide Fold Belt part in the ~500 Ma Delamerian Orogeny (Fig. 1, Foden et al., 2006; Foden et al., 2002; Weinberg et al., 2013). The area is dominated by a thick, turbidite sequence known as the Kanmantoo Group (Jago et al., 2003). This sequence is both the source and the host of a number of granite intrusion and migmatites (Foden et al., 2002). The intrusive granites range from transitional S/I-type granites to pure crustal S-type granites (Foden et al. 2002), which intrude and mingle with migmatites, indicating a contemporaneous evolution (Schwindinger and Weinberg, 2017). These migmatites were interpreted to have

formed by a combination of muscovite-dehydration and water-fluxed melting with up to 1 wt.% excess H_2O (Schwindinger and Weinberg, 2017; Schwindinger et al., 2018) at temperatures < 700°C and pressures below 5 kbar (Mancktelow, 1990). The small amount of excess H_2O increased fertility, resulting in melt fraction in excess of 20 vol.% and formation of diatexites. The map in the Electronic Electronic Appendix 1 shows the location of the outcrops between Stun'Stail Boom River and Vivonne Bay and the position of all samples used here.

Lithologies

The main migmatitic and magmatic rock types exposed on the south coast of Kangaroo Island are briefly described here. Following the classification of Sawyer (2008) migmatites are divided into diatexite and metatexite, based on whether or not the rock maintained coherence and preserved pre-anatectic structures.

Metatexite

Metatexite preserves layering between grey feldspathic psammites and dark, biotite-rich pelitic beds in the turbidite (Fig. 2a). Leucosomes in the metatexite are usually less than 2 cm wide. Structurally, leucosomes occur in different orientations. Most of them follow bedding, but some follow orientations defined by shear-bands, axial planes of folds, or form isolated pockets of melt. This diversity in orientations and styles give rise to patch, stromatic and net-structured metatexite (Sawyer, 2008). Leucosomes have a wide compositional variation, reflected by variable proportions of K-feldspar, ranging from common tonalitic leucosomes to rarer granitic ones, and scarce alkali feldspar-granite leucosomes. Variation occurs on many scales, and even single outcrops and single leucosomes show along-strike variation in their assemblage modal proportions (Section 3). In addition, some leucosomes have mafic selvedges surrounding them, comprising coarse biotite, plagioclase and minor

muscovite, and rich in accessory minerals (Fig. 3b). Domains in metatexite that are dominated by residual minerals, such as biotite are referred below as residual layers, while leucocratic rocks with small melt patches, such as biotite-poor psammites are here referred to as anatectic psammites.

Diatexite

Diatexite is characterized by irregular remnants of disaggregated metasedimentary rock in a magmatic matrix (Fig. 2b), and are indicative of a large former melt fraction. The remnants of the source comprise centimetre- to metre-sized schollen, schlieren and biotite clots down to single grains, giving the rock a strongly heterogeneous appearance. Diatexites that developed in sources dominated by biotite-poor psammite, are chemically controlled by their unmelted precursor, and therefore described as psammite-rich diatexites. In general, diatexites are exposed on up to 3 km-long strips of coast, typically associated with and intruded by granites (see map in Electronic Appendix 1).

Intrusive granites

These are medium- to coarse-grained biotite-granites with rounded, hexagonal or rectangular K-feldspar megacrysts, reaching 5–10 cm across (Fig. 2c). Compared to the diatexites, the intrusive granites have coarser grain size and lack direct evidence for *in situ* disaggregation of source lithologies. However, the presence of rectangular to rounded xenoliths of typical Kanmantoo Group rocks, also suggests strong contributions of the Kanmantoo Group in their generation. They also have preserved blocks of older phases of a similar granite with only small textural differences. These granites crop out as several headlands and coastal sections of up to 1.5 km in length.

Leucogranites

Leucogranites are spatially associated with migmatites and comprise centimetre- to several metre-wide dikes and sills, which are locally in petrographic continuity with leucosomes in country rock. They typically contain muscovite, garnet or tourmaline and the largest leucogranite body mapped was a 300 m long coastal section and resulted from the merging of multiple sheets, each 20–50 cm wide, that vary in grain size and mineralogy (Fig. 1d). In contrast to megacrystic granites, the leucogranites lack K-feldspar megacrysts biotite is absent, except for a small number of biotite-bearing leucogranite sills in metatexite in the far west of the mapped area (Schwindinger and Weinberg, 2017).

Tonalite dikes

Two ~1 m-wide dark grey tonalite dikes that are interlayered with leucogranite (Fig. 1d) are mineralogically similar to diatexites, but have a more homogenous texture, lacking schollen and biotite clots. In thin section they have a touching framework of plagioclase grains with interstitial quartz and rare K-feldspar. Biotite is homogeneously distributed and has numerous accessory mineral inclusions (monazite, xenotime, zircon). Contacts between the tonalites and surrounding leucogranite have lobate geometries with diffuse margins and disaggregated and stretched pillows of one in the other near the contact, indicative of co-magmatic relationships (Fig. 1d).

FRACTIONATION OF LEUCOSOMES WITHIN THE SOURCE

Here, we describe a connected leucosome-dyke network (Fig. 4) in the metatexites of Vivonne Bay that evolves in shape and mineralogy over a few metres indicating a transition from an extraction network to an intrusive network. The exposure of a single connected system is rare, however it is common to find different parts of these system exposed in the same outcrop (Weinberg et al., 2013). They are particularly common in the metatexites of

Vivonne Bay area, but less common in the diatexite-dominated regions to the west (see map in the Electronic Appendix 1).

The connected leucogranite network is preserved in a folded sequence of psammo-pelite and psammite layers (Fig. 4d). At one end, the root, the network is characterized by dendritic leucosomes rooted in the rock matrix of the psammo-pelitic layer into which they disappear. In the other direction, away from their roots, the dendrites link to form planar dikes at the contact between the psammo-pelite and the psammite. This in turn becomes a set of angular quartz veins that ends in branches with sharp tips against the country rock. All of this occurs within 3-5 metres and is accompanied by a gradual change in leucosome composition. In the root zone, small isolated patches of former melt, comprising plagioclase and quartz, merge into a continuous stromatic tonalitic leucosome with diffuse boundaries with the surrounding metasedimentary rock (Fig. 4a and Fig. 5a,b). Plagioclase grains in this tonalitic leucosome form cumulate texture with a network of subhedral touching grains with interstitial quartz (Fig. 5b). Further in the network the leucosomes have more defined boundaries and narrow biotite-rich selvedges. The presence of K-feldspar is first documented in the zone of merging leucosomes that form a 5 cm wide granite (Fig. 4b and Fig. 5c). The dike is coarse-grained and cuts through the contact at a high angle with sharp contacts with the surrounding psammite beds (Fig. 4b and Fig. 5d). The granite can be followed for a few metres, after which it splits into several, irregular quartz veins (Fig. 4c).

This network indicates that magma crystallized and fractionated over a few metres. Magma crystallization impacts on the saturation of accessory minerals, thus controlling the behaviour of U, Th, Y, Zr and REE. Whole rock geochemistry will be investigated in the next section with the aim of understanding the fate of these elements and their related accessory minerals.

ACCESSORY MINERAL DISTRIBUTION AND CHEMISTRY

In order to determine the behaviour of accessory minerals and the fate of U, Th (heat producing elements), Y, Zr and REE, the distribution of accessory minerals in thin section was analysed in three different samples and the composition of these minerals was determined with focus on these elements. This mineral chemistry information is integrated with migmatite whole rock geochemistry.

Methods

Three analytical methods were used here: mapping the distribution of accessory minerals in thin section using backscattered electron microscopy (BSE), analysis of their trace elements using LA-ICP-MS, and determination of whole rock geochemistry using XRF and ICP-MS. Three thin sections representative of different migmatite rock types were selected for investigation of accessory minerals and to allow for later comparisons with whole rock geochemistry. Two of these samples are metatexites, each composed of three domains: leucosome, biotite-rich selvedge and mesosome (6ML1_1 and 6ML1_6; Figs. 2a-c). These samples record processes that are related to partial melting and melt segregation. The third thin section is from a diatexite, reflecting magmas that are strongly contaminated with residual material (6ML21_1, Fig. 3d).

Backscattered electron maps of the thin sections were carried out at the Monash Centre of Electron Microscopy (MCEM) on a JEOL7001F FEG scanning electron microscope equipped with an Oxford Instruments X-Maz 80 EDS detector. The bright accessory minerals in BSE images were automatically selected by setting a greyscale threshold during acquisition. For each detected accessory mineral grain the geometric properties were measured (e.g. diameter, area) and a qualitative composition was determined using a 1s EDS spot analyses in the centre of the selection in order to positively identify the mineral (the different stages of data acquisition are shown in Fig. 6).

The accuracy of this method depends on the resolution of the mapping, which varied between samples. The final resolution used was 2 pixels/μm, allowing confident detection of all grains larger than 3 μm in diameter. The fact that smaller grains have not been detected, is inferred to have only minor effects to this study, because: (a) most grains range between 10 and 40 μm with less than 10% of the cumulative grain area in grains below 10 μm (Fig. 7), and (b) following from a) the contribution of the smallest grains to the bulk concentration of trace elements in the rock is only marginal. We focus only on the most common accessory minerals: apatite, monazite, xenotime and zircon, because the modal proportion of other detected accessory minerals (e.g. very rare uraninite in leucogranite) is negligible. Further errors arise from low contrasts in BSE images between different accessory minerals or between rock-forming minerals and their accessory inclusions, causing grains not to be detected as separate ones or incorrectly classified. Apatite, because of its lower contrast against rock-forming minerals, was particularly problematic and had to be digitized manually in samples 6ML1_6 and 6ML21_1, using ImageJ on the high resolution BSE map. In addition, single grains are occasionally split by the program into separate ones if grains were cracked or not homogeneously polished, causing the greyscale pixels in the BSE image to locally fall below the threshold. This can bias the grain size distribution towards smaller sizes. For this reason, the cumulative area of grains was used instead of absolute grain sizes. An exception is Fig. 7 where grain size in different domains of the migmatite sample are compared. We estimate the vast majority of accessory grains exposed at the surface of the studied thin section have been detected. Later in the text we will see that using the modal proportion of accessory phases we were able to closely predict bulk rock composition in the elements controlled by these phases, giving us confidence that selected samples are representative of the different rock types in the outcrop.

Trace element compositional analysis of accessory minerals was conducted at the Monash Isotopia Laboratory using an ASI RESOlution SE 193 nm ArF excimer laser equipped with a Laurin Technic S155 ablation cell coupled to a Thermo Fisher Scientific iCapTQ. The general small grain size of the accessory minerals in the thin sections restricted the analyses to apatite, zircon and monazite. Xenotime typically had a diameter below 20 μm, impeding LA-ICP-MS analyses. Apatite and monazite have been measured using an energy of 6 mJ and a spot size of 15 μm, whereas zircon has been measured using 4 mJ and 25 μm. NIST610 was used as calibration standard (Si for zircon, Ca for apatite, P for monazite), and NIST612 was used as a quality control sample. The overall accuracy is 5 % deviation from reference values for NIST612. Phosphorous required for the internal standardization of monazite, was not measured in sufficient quantities during the runs, which led to inaccurate results for monazite. Therefore, for both monazite and xenotime, the mean concentration of EDS measurements during the scans were combined with several additional, more accurate, single spot EDS measurements to obtain an average composition of these minerals in their respective major elements. Their trace element concentration was not measured.

For whole rock geochemistry, fresh samples were crushed and milled using a tungsten-carbide mill. Major element analyses were conducted at the Centre of Excellence in Ore Deposits (CODES), University of Tasmania, Australia, on a Panalytical Axios Advanced 4.0 kW X-ray Fluorescence (XRF) Spectrometer. Trace element analyses of all samples were conducted at Monash University Isotopia facility, using sample solutions on a Thermo Finnigan X series II, quadrupole Inductively Coupled Plasma Mass Spectrometer (ICP-MS). Details of analytical procedures are provided in Electronic Appendix 2.

Results

Bulk Rock Geochemistry

Whole rock major and trace element composition was acquired for 31 samples (Table 1). The results were combined with existing datasets of magmatic rocks (Foden et al., 2002; Tassone, 2008) and lower grade Kanmantoo Group metasedimentary rocks (24 samples, Haines et al., 2009; Turner et al., 1993). Leucosomes and leucogranites are grouped together as felsic granitoids, and are different from granitoids which have a higher proportion of biotite (>5% modal), such as diatexites, granites and tonalite dikes.

Major and REE geochemistry

All samples are peraluminous with an aluminium saturation index (ASI) > 1.1 (Table 1, Fig. 8a) and silica contents of 65–80 wt.%. The residual biotite-rich layers, have the lowest SiO_2 values, whereas psammites have the highest values. $MgO+FeO_T$ is negatively correlated with SiO_2 with two trends identified (Fig. 8b): (i) a linear trend linking residual layers with the most silica-rich samples, interpreted to represent different degrees of melt-residuum separation (Foden et al., 2002); and (ii) a weakly-curved trend defined by felsic granitoids (orange symbols in Fig. 8b) at ~74 % SiO_2 involving decreasing values of $MgO+FeO_T$ (Foden et al., 2002). This second trend is more pronounced in the $MgO+FeO_T$ vs. K_2O plot in Fig. 8c, where leucosomes and leucogranites spread from 3 to 7 wt.% K_2O at the bottom of the diagram. This trend corresponds to the fractionation described in Section 3, from cumulate tonalite at one end of the trend to potassic granites at the other end. Leucosome sample SSBR22 plots in the centre of this trend at 4.5 wt.% K_2O, and is considered the best representative of an anatectic melt. This is because it lacks cumulate textures, has few obviously residual minerals, and lacks an Europium anomaly (Eu/Eu* ~1).

Figure 8c shows a second subhorizontal trend defined by anatectic, plagioclase-rich psammitic diatexites (grey symbols). These are silica-rich (~80 wt.%) rocks rich in psammite blocks with small but variable quantities of muscovite, biotite and little K-feldspar. Diatexites

and granites define a third trend that evolves diagonally away from the centre of Kanmantoo Group field towards the leucosome sample SSBR22, at higher K_2O and lower $MgO+FeO_T$. This reflects the partial removal of residual solids from the flowing magma and possibly mixing between anatectic magmas and intrusive granite as suggested in Foden et al. (2002) and Schwindinger and Weinberg (2017). Residual layers are characterized by the loss of granitic melts and plot towards the biotite corner of Fig. 8c. For comparison, Fig. 8d plots the composition of migmatites and granites generated by melting of the turbidites form the Sierra de Quilmes in NW Argentina. These were produced by biotite-dehydration melting reactions at 800-850°C (Büttner et al., 2005; Finch et al., 2017; Wolfram et al., 2018). Despite their higher temperatures and different melting reaction, they show similar trends to Kangaroo Island migmatites, in particular the horizontal fractionation trend at the base of the diagram (Wolfram et al., 2018). One difference is that the residual migmatites in Sierra de Quilmes trend towards the garnet and cordierite side of the diagram, which is absent from Kangaroo Island where these minerals are lacking.

Diatexites, granites and residual layers have similar total REE concentration, plotting over the field of unmelted Kanmantoo Group (Fig. 9a). Psammite-rich diatexites have slightly lower total REE. Felsic granitoids are depleted in LREE compared to the Kanmantoo Group with a subtle positive HREE, including HREE enrichment of a few leucosomes above the source (Fig. 9b). The tonalite dikes have LREE comparable to the Kanmantoo Group, but are strongly enriched in HREE. The europium anomaly of all these granitoids is either positive or negative, depending on the total REE concentration, but not far removed from those of the source rocks.

Other Trace Elements

Accessory minerals, such as zircon, monazite, apatite and xenotime, are the main hosts of REE, Zr, Y, Th and U in psammitic and pelitic metasedimentary rocks (Bea, 1996). The behaviour of these minerals during partial melting therefore strongly controls their concentration in the resulting granite magmas. Here, these elements are plotted against $MgO+FeO_T$ (Fig. 10) to determine their behaviour relative to melt and residuum. The data in the plots can be roughly divided into two sections: above and below $MgO+FeO_T$ ~2.7 wt.%, which corresponds to the boundary between felsic granitoids and other rock types. Rocks above this value are typically diatexite or granites, and their trace elements define a plateau that mostly coincides with the values of the Kanmantoo Group. Below this value, felsic granitoids are poorer in ΣLREE, Th and Zr with decreasing $MgO+FeO_T$ (Fig. 10a-c).

Felsic granitoids plot close to the 650°C Zr-saturation line for peraluminous melts or below, suggesting an undersaturation of the initial higher temperature magma in Zr (Fig. 10a). An exception is the leucosome representative of anatectic melt, SSBR22, which plots closer to the 700°C saturation. The behaviour of Th and ΣLREE are similar to that of Zr (Fig. 10b,c). Granites, diatexites and residual rocks plot at an elevated plateau of ΣLREE, close to 150 ppm, inside or slightly above the Kanmantoo Group field. With a decrease in $MgO+FeO_T$, reflecting a decrease in biotite mode, the ΣLREE values also decrease. The maximum value for leucosomes is recorded by sample SSBR22 at 70 ppm and corresponds to a ΣLREE saturation temperature of ~670°C.This behaviour is also found in rocks of the higher temperature anatectic turbidites of the Sierra de Quilmes (Fig. 10d, Wolfram et al., 2018).

Uranium lacks a clear trend when plotted against $MgO+FeO_T$ (Fig. 10e). The same is true for (Fig. 10e) ΣHREE or Y versus $MgO+FeO_T$ (not shown, values provided in Table 1). These elements generally have similar values to those of the Kanmantoo Group, which probably relates to the complex behaviour of multiple U- and ΣHREE-bearing minerals (Bea,

1996). The most enriched samples are the tonalite dikes and even some leucosomes have values slightly higher than most other rocks. In addition, the strong correlation of these three elements, in particular Y with ΣHREE, suggests that they may be controlled by xenotime (Fig. 10f).

Accessory mineral imaging

Using high-resolution BSE maps, a precise determination of the textural location, grain size and qualitative composition of all accessory minerals in the three thin sections was carried out. Figure 5 details the results for sample 6ML1_1 (maps of other samples are provided in Electronic Appendix 3). Accessory minerals are not distributed homogeneously but show a strong variation in their modal proportions between the different domains (Fig. 6c) with the leucosome having only a fraction of the accessory minerals of both the selvedge and the mesosome surrounding it.

Quantification of the distribution of accessory minerals in each domain (Table 2) shows that the leucosome is indeed impoverished in accessory minerals and has the lowest modal proportions of accessory minerals (Fig. 6d). By contrast, the selvedge, which only covers ~12 % of the total scanned area, has 15 times the accessory mode of the leucosome. The largest and most abundant accessory mineral across all domain in sample 6ML1_1 is apatite, representing ~80 % of the area of all accessory mineral with a modal abundance of 0.15 %, followed by zircon (12 % of grains), monazite (7 %) and a small fraction of xenotime (<1 %, Fig. 6d), consistent with the general abundance in the other scanned sections (Table 2). The majority of grains range between 10 and 40μm in diameter, independent of their location. Large grains between up to 100 μm have a tendency to be located in the selvedge and to a lesser extent in the mesosome, but are rare in the leucosome (see Fig. 7 for zircon grain size distribution in 6ML1_1).

Each grain in the thin sections was classified based on its textural location (Table 2, Fig. 11). Six different categories were defined: inclusions in each of the main rock-forming minerals (biotite, quartz, plagioclase, muscovite, K-feldspar) and grains that are on biotite grain boundaries in contact with either quartz or plagioclase. Accessory grains located on grain boundaries between the same two minerals, e.g. in between two plagioclase grains, were treated as plagioclase inclusions. As expected, most grains are associated with biotite, either as inclusions or at biotite grain boundaries (Fig. 11b). Even in the biotite-poor leucosomes, ~70 % of all accessory grains are in contact with this mineral. The selvedge is composed almost entirely of biotite with only minor plagioclase, quartz and feldspar, hence ~70 % of all grains are biotite inclusions and another 20 % are found at the edge of biotite grains. The distribution of accessory minerals in the mesosome is similar to that in the leucosome, but with a more equal distribution between the major minerals, including ~18 % both in quartz and plagioclase. The textural location of accessory minerals in the second metatexite sample 6ML1_6 is comparable to 6ML1_1, but has coarser grained plagioclase in the leucosome hosting a greater total volume of accessory minerals. The diatexite sample 6ML21_1 is similar to the mesosome in Fig. 11b, but contains K-feldspar that hosts ~3 % of all accessory minerals (Electronic Appendix 4).

Mass balance

The cumulative area covered by each accessory mineral is combined with their composition (Tables 2 and 3) to calculate their contribution to the whole rock trace element concentration which can then be compared to measured values. LA-ICP-MS trace element data was collected for zircon and apatite as they comprise over 90% of the total accessory minerals. The data show no systematic relationship between the domain location of these minerals (leucosome, selvedge or mesosome) or between samples and their trace element concentration. This is shown for U/Th and ΣREE in Fig. 12a, but is also true for other

elements such as Y, or Zr. Therefore, the average composition was used for further calculations (Table 3). Monazite and xenotime were analysed using EDS, which only yielded information on elements with concentrations above 0.5 wt.%. The detected elements include Y, La, Ce, Nd, Th, U for monazite, and Y, Yb, Th, U for xenotime. We used the average value for these elements in monazite and xenotime for each sample based on more than 100 analyses each (Table 3). The distribution of key elements in the accessory minerals in sample 6ML1_1 in Fig. 12b shows that Zr is effectively entirely hosted by zircon, whereas monazite hosts >90 % of LREE and Th. Unlike the other elements, U resides in different minerals and apatite contains 90 % of all P_2O_5, as a result of its high modal content in the rock. Xenotime, the least abundant mineral, is the main host of Y. In addition, the good correlation between Y and HREE (Fig. 10f) further suggests that xenotime is an important host of HREE, which is supported by the study of Hammerli et al. (2016) from another section of the Adelaide Fold Belt.

Combining the measured area of each accessory mineral in Table 2 and their trace element concentration, we calculated the composition of each domain via mass balance. The results for sample 6ML1_1 (Table 4; comprehensive results in Electronic Appendix 5) show that the leucosome has the lowest concentration of LREE, Zr, U, Th and Y, while the mafic selvedge has the highest, in good agreement with the ranges found in whole rock geochemical analyses of different groups of rocks in the area (Fig. 13). The difference between domains in Sample 6ML1_6 is less well-defined because the domains themselves are more diffuse. Nevertheless, results follow the general pattern of having REE- and HPE-poor leucosomes and HPE-rich residual layers (Table 4).

DISCUSSION

Migmatites in vast turbidite sequences accretionary orogens typically contain a variety of leucosome types even within single outcrops (Finch et al., 2017; Sawyer, 2008; Watson, 1988; Watson and Harrison, 1984). Further to that, leucosomes are commonly impoverished in elements such as U, Th, Y and REE, compared to their sources, most typical for melting below T<850°C, but also described in terrains undergoing biotite dehydration melting at temperatures >850°C (Bea, 2012; Sawyer, 1991; Villaseca et al., 2007; Watt et al., 1996; Wolfram et al., 2018). However, in some such terranes the behaviour of these elements is inconsistent and can vary locally (e.g. in the Wuluma hills or the Ashuanipi terrane, Clarke et al., 2007; Guernina and Sawyer, 2003) and the Kangaroo Island migmatites are no exception. Below we demonstrate that both these features result from a common process. We will first discuss the bulk rock evolution of the Kangaroo Island migmatites and then explore *in source* fractionation and crystallization of melt as evidenced by Fig. 4 and how they control the behaviour of accessory minerals during magma evolution within the source.

Bulk rock evolution

The compositional variation of granites has traditionally been described as the superposition of several processes, which are roughly divided into those that modify an initial melt by hybridization, either with other magmas or with solids, and those that are related to the chemical differentiation of the magma. The magmatic rocks of the Kangaroo Island indicate that both types of processes contributed to their evolution.

The diatexites have variable contents of residual minerals derived from the disaggregation of the source (Fig. 3) and consequently have compositions between the field of the Kanmantoo Group protoliths and samples representative of melt (such as SSBR22, Fig. 8b,c). Variable melt–residuum separation leads to typically linear geochemical trends in diatexites between protolith and melt (Foden et al., 2002; Milord et al., 2001; Solar and

Brown, 2001; Wolfram et al., 2018). Intrusive granites plot along the same trend but stretch to higher K_2O and lower $MgO+FeO_T$, reflecting more efficient melt–residuum separation, and possibly some mixing with more pure anatectic melts (Foden et al., 2002). Both granites and diatexites have REE concentration that coincide with the range of values of the Kanmantoo Group in Fig. 9, further supporting the kinship to this source.

The compositions and geochemical trends defined by the leucocratic granitoids contrasts with those of diatexites. The leucocratic suite varies in composition from tonalites to granites and define the curved trend to lower $MgO+FeO_T$ with increasing silica, branching off from the main trend in Fig. 8b. They additionally define the subhorizontal spread in the $MgO+FeO_T$ vs. K_2O plot (Fig. 8c) and vary in REE contents, with a tendency of K_2O-poor tonalite dike samples to be enriched in HREE, while the potassic endmembers are generally impoverished in REE (Fig. 9b). The geochemical trends of these leucocratic magmatic rocks are reflected in small scale by the documented modal changes along the connected leucosome networks in metatexites depicted in Fig. 4.

Fractionation of leucosomes within the source

Section 3 and Fig. 4 showed that the continuous leucosome networks display a compositional range from plagioclase-rich leucosomes, interpreted as early crystallized felsic cumulates, to K-feldspar-rich leucosomes and quartz veins, interpreted as crystallized from the fractionated melt (Kriegsman and Hensen, 1998; Sawyer, 1987). Given the rooted nature of the network within the source rock, and given the short distance in which this occurs, we interpret this network to record a simultaneous process of melt extraction from the source and its crystallization and fractionation during extraction in a hot environment. If this is the case, declining temperatures alone do not explain crystallization. So how did the magma crystallize?

White and Powell (2010) pointed out that the preserved leucosome mineralogy not only depends on pressure, temperature and protolith compositions, but also on diffusion of mobile elements, especially with the host rocks along chemical gradients that arise from changing *P–T*. The authors thus explained the origin of anhydrous leucosomes with biotite-rich selvedges. We use the concept of White and Powell (2010) to explain *in source* crystallization of magma, and extend to chemical gradients that arise from changes associated with melt flow through different lithologies, including variations in H_2O activity and chemical potential throughout the rock mass.

The volume of rock and melt in equilibrium with each other or attempting to equilibrate in a complex anatectic system is generally unknown (Guevara and Caddick, 2016; White and Powell, 2002, 2010) and depends on rates of diffusion of different species, the physical distribution of melt in the host rock, and the rates of melt migration and extraction, all of which vary in space and time. A small melt batch might be in equilibrium with its reactants at the grain scale, but might define a local environment slightly different from the next small batch, particularly with regards to communication and equilibration with heterogeneously distributed accessory minerals. Melt migration brings these small batches together in the roots of leucosomes, where they partly homogenize. As migration continues they encounter compositional domains within the suprasolidus source different from those in which the melt originated, such as migration from a pelite host rock to psammite (Fig. 5d), and/or variable H_2O activity (aH_2O), related to heterogeneous distribution of H_2O content, either from variable availability of a free aqueous fluid or silicate melts with different concentrations of dissolved H_2O in the interstices of the rock. Here is where chemical gradients between melt and rock emerge and diffusional exchange is required to balance these, similar to gradients that arise through P-T changes of the system (Guevara and Caddick, 2016; Nicoli et al., 2017; White and Powell, 2010). Diffusion of the mobile species

K_2O, Na_2O and H_2O happens relatively quickly within a melt-bearing system and are likely to show the largest effects (Acosta-Vigil et al., 2006; Acosta-Vigil et al., 2005; Morgan et al., 2008). These imbalances may be particularly pronounced and cause significant crystallization if they are triggered by local and wide variations in aH_2O. In a long-lived system of varying P-T-aH2O, in which magmas migrate across a layered package, the moving magmas will be constantly in the process of equilibration with the surroundings, crystallizing and fractionating when the conditions require.

For the leucosome network in Fig. 4, changes associated with the transition from the K_2O-rich psammo-pelite to the Na_2O-rich psammite, combined with possible differences in aH_2O, caused chemical gradients to emerge. Ensuing equilibration may have triggered crystallization and fractionation as the magma flowed. The absence of K-feldspar in the tonalitic leucosomes of the psammo-pelite part of the network can be interpreted as caused by diffusion of K_2O and H_2O to the host, causing biotite to grow in the selvedge, while the leucosome crystallized plagioclase and quartz (White and Powell, 2010). We postulate that the melt that managed to leave the psammo-pelite host, entered an environment with a marginally higher solidus temperature and lower aH_2O in the psammite. This favoured loss of H_2O to the surroundings, which initiated crystallization of the coarse-grained granite. Because of the less aluminous and less ferro-magnesian nature of the psammite host, melt did not lose K_2O through diffusion to grow new biotite, and instead crystallized K-feldspar. The angular quartz veins at the final tips of this system precipitated from silica-rich liquids that segregated after all granite melt crystallized.

An alternative and perhaps more standard interpretation would be that the crystallization of the leucosome network in Fig. 4 records the cooling of the migmatites across the solidus (Sawyer, 1987). This is possible but we note that this would imply that the network records the cooling history of the migmatites, from early cooling and tonalite

crystallization to quartz veins formation at some 200ºC cooler conditions. The further implication is that the network crystallized diachronously, potentially over a few million years of cooling history.

Fate of accessory minerals

Section 4 showed that the Kangaroo Island anatectic leucogranites have lower contents of Zr, U, Th, Y and LREE relative to their likely source rocks, suggesting that partial melting or fractionation of magmas were unable to enrich the peraluminous rocks in these elements. As we have seen in Fig. 12, monazite, zircon and xenotime control the distribution of U, Th, REE, Y and Zr (Bea, 1996b), and the distribution of these elements and of accessory minerals are related to the biotite content in the rock (Fig. 10)

The dissolution of accessory minerals during anatexis and their precipitation from a melt depends on multiple related factors, such as the composition of the melt (Bea et al., 1992; Spear and Pyle, 2002; Wolf and London, 1994), P-T conditions (Montel, 1993), water content of the melt (Boehnke et al., 2013; Montel, 1993), reaction kinetics (Rapp and Watson, 1986), or disequilibrium caused by rapid melt extraction (e.g., Clemens and Stevens, 2016). As shown by White and Powell (2010) local disequilibrium and diffusion along chemical gradients within a system have also the potential to affect when and where accessory minerals are dissolved and when they precipitate.

The Kanmantoo Group contains Zr and LREE contents in excess of the saturation concentration in peraluminous melts at peak temperatures of 700°C (Fig. 10). This would allow melts to become saturated in these elements before all zircon, apatite and monazite (hosting LREE) in the source became dissolved (Yakymchuk and Brown, 2014).

Nonetheless, the felsic granitoids in Fig. 10 plot below the calculated saturation concentration for Zr and LREE, and have low Th values, whereas diatexites, granites and tonalite dikes, all richer in biotite, plot at higher values broadly coincident with those of the Kanmantoo Group field (Fig. 10). The sample that is the closest representative of an anatectic melt (SSBR22) has Zr and LREE concentrations corresponding to saturation at 700°C (Boehnke et al., 2013) and 675°C (Stepanov et al., 2012), respectively, consistent with the estimated peak metamorphic temperatures in the area. We have previously described the two distinct trends in Fig. 10, a scattered horizontal one above 2.7% $MgO+FeO_T$, and a positive trend defined by felsic granitoids below this. In order to detail the trend in Fig. 10 we plotted the trace elements against each other in Fig. 14.

With the exception of the felsic granitoids, Fig. 14a shows a broad sympathetic increase in Zr with LREE indicating zircon and monazite become enriched together in the more residual rocks enriched in $MgO+FeO_T$, most likely because of their direct physical link with biotite (see Fig. 11). It also shows that the calculated compositions based on the accessory mineral concentrations of the three domains in 6ML1_1 (leucosome, mesosome, selvedge in Fig. 13) closely match the main trend of whole rock composition. By contrast, the calculated values for diatexite sample 6ML21_1 and metatexite sample 6ML1_6 deviate from the trend in Fig. 14a with lower values of ΣLREE, but match whole rock Th and U in Fig. 14b. The underestimation in ΣLREE and Zr for the diatexite is likely caused by the limited area investigated in a single thin section, failing to reflect the complete heterogeneity of diatexites, while the ΣLREE underestimation for sample 6ML1_6 is unclear, but possibly relates to the exclusion of xenotime in the calculations, which is more abundant in this sample (0.004% modal percent compared to 0.002% in 6ML1_1, Electronic Appendix 4).

The felsic granitoids are all poor in Zr, Th and LREE and tend to define slightly different trends in Fig. 14 (particularly in Fig. 14c) reflecting their different behaviour in Fig.

10. This can be because: (a) melt was undersaturated initially, (b) these elements diffused from the melt when accessory phases grew in surrounding solids, or both. An initial undersaturation in LREE and Th in the melts can be explained by the much higher solubility of apatite compared to monazite and xenotime in peraluminous melt, causing melt to saturate in P with respect to monazite and xenotime (Rapp and Watson, 1986; Wolf and London, 1994; Wolf and London, 1995), therefore stabilizing the main repositories of Th, LREE (monazite) and U, Y (xenotime) in the source. This has been used to explain anatectic magmas similarly impoverished in LREE and Th (Fig. 10d, Wolfram et al., 2018). However, this mechanism cannot explain the undersaturation in Zr. Watson et al. (1989) suggested the possibility that accessorises may be physically isolated from the melt because of their inclusion in stable major rock-forming minerals, such as biotite, but as Fig. 11 shows, a third of all accessory minerals in the mesosome are located at the grain boundary of biotite, which would allow melt to dissolve sufficient quantities of these to reach saturation. Therefore option (b) is a more plausible explanation for low Zr concentration and could exacerbate impoverishment of Th and LREE in the felsic granitoids. Further to that, this process would explain why the selvedge is so enriched in accessory minerals compared to mesosome.

As a magma crystallizes in part due to chemical interaction with its host within the source region (Fig. 5d), it becomes saturated with respect to Zr, Th and LREE leading to crystallization of the host minerals of these elements — the accessory minerals. Their enrichment in biotite-rich selvedges (Fig. 11), suggest that they crystallize preferentially on biotite, as also found by earlier studies describing heterogeneous nucleation of accessory minerals (Bacon, 1989; Bea, 1996b; Wolf and London, 1994). This process explains the apparent undersaturation of the leucosomes (Figs. 9 and 14): as melt crystallizes, either from reaction with its host rock or decreasing temperature to form evolved granitic rocks, it tracks the saturation curve of LREE, Th, Zr and Y and depletes the final magmatic rock in these

elements because the accessory minerals crystallize in the biotite selvedge outside the leucosome. Thus, the spatial arrangement of the melt network in the anatectic zone and the residence time of melt in this region will influence the content of LREE, Th, Zr and Y in the melt and crystallizing leucosomes. This process would be most efficient in small magma volumes with short diffusional distances to the country rock.

The behaviour of phosphates can be further investigated in plots of Th and Y against P_2O_5 (Fig. 14c,d), which show three different trends. The green, diagonal arrow in Fig. 14c defines a trend towards magmas with increasingly higher proportions of residual components including their accessory minerals. Felsic granitoids define a horizontal trend towards high P_2O_5 at the bottom of the diagram (red arrow in Fig. 14c). Low Th and Y along this trend indicate these samples have few monazite or xenotime grains, which we argue is due to the crystallization of these minerals in the selvedges. The trend to higher P_2O_5 suggests that apatite, the main host of P_2O_5, is not removed by this process, and agrees with the high solubility of apatite in peraluminous magmas (Bea et al., 1992). A third, subvertical trend in Fig. 14c,d (blue arrow) is defined by the tonalite dikes, plus a single diatexite sample and a leucosome with tonalitic composition. This trend combines high Th and Y at low P_2O_5, and indicates that these rocks have higher proportions of monazite and xenotime. This is also reflected in the high HREE of the tonalite dikes in Fig. 9. These rocks possibly record a different type of behaviour of the magmatic system: one in which monazite and xenotime are not lost to the melanosome, perhaps due to fast extraction, but accumulate in these magmatic rocks. An explanation for this behaviour could be the relatively rapid accumulation of magma batches that are large enough to be isolated from the country rock. Here, they are unable to lose significant amounts of the HREE via accessory mineral crystallisation in the hosting selvedges, and so form these minerals in the early crystallized cumulates. The rare

preservation of such rocks in the area, with only two narrow tonalitic dikes observed, however indicate that this behaviour is not very common.

In summary, the geochemical investigation of the Kangaroo Island magmatic rocks indicate that felsic granitoids with little residual source material are poor in HPEs (U, Th), Zr, Y and REE. This could have been caused by two parallel processes: (a) melt may have been initially depleted as a result of the low solubilities of REE-Y phosphates because of preferential dissolution of apatite and saturation of P in the melt (Wolfram et al., 2018); and (b) crystallization of accessory minerals in the selvedges, effectively removing the key trace elements from the melt by diffusion, due to emerging chemical gradients between magma and surroundings.

The most obvious way to increase the concentration of trace elements in the magmatic rocks is to add residuum, shown by diatexites and granites loaded with solids from the disaggregated source. In this case the concentration of trace elements in question is capped by the maximum value of the Kanmantoo Group source, unless there are processes that concentrate residual or newly crystallized accessory minerals. This is observed in the tonalite dikes enriched in U, Th, Y and HREE, which suggest the possibility that if larger magma batches are accumulated and experienced little interaction with the host rocks, the trace elements that form accessory minerals are not lost and can subsequently be enriched in crystal-rich magmas.

Implication for crustal differentiation

Turbidites such as those forming the Kanmantoo Group, form vast volumes of material that are added to the accretionary orogens where they are strongly reworked at high-T/low-P conditions and ultimately become part of the crystalline continents (Cawood et al., 2009; Weinberg et al., 2018). While partial melting and magma extraction to higher levels are

generally considered the main differentiation process of the crust (Brown, 2013; Brown and Rushmer, 2006; Sawyer et al., 2011; Taylor and McLennan, 1995), we argue that because of the nature of the anatectic process recorded by turbidites in such orogens, intracrustal differentiation is unlikely to contribute significantly to the redistribution of U, Th, Zr, Y (Yakymchuk and Brown, 2019).

The processes documented by the anatectic metaturbidites of Kangaroo Island, echoes those occurring at higher temperature in other regions where melting was a result of biotite-dehydration reactions at 800– 850°C (e.g. the Puncoviscana Formation in NW Argentina shown in Fig. 10d, Büttner et al., 2005; Wolfram et al., 2018). Despite the temperature differences, in both cases the majority of granitic magmatic rocks produced had either similar or lower contents of U, Th, Zr, Y and REE, compared to their sources (Figs. 10 and 14).

Close contact between narrow segregation channels and solids lead to accessory growth in melanosome. If melanosome and magmas become ultimately separated, rather than mobilized together, the processes documented here will cause undersaturation of the magma in elements typical for these minerals with significant impacts on granite composition and implications for transfer of the two most important HPE: Th and U. This finding is consistent with those of Alessio et al. (2018) and later by Yakymchuk and Brown (2019) who showed that heat production rates in metapelites that underwent considerable melt loss were either the same or higher than those in equivalent subsolidus metapelites. This implies that U and Th have not been preferentially extracted with the melt, and might even have been enriched in the source. Consequently, the source regions of these crustal magmas remain hot for extended periods, unable to cool and thermally stabilize the lower crust (Sandiford and McLaren, 2002). This coincides with geochronological studies of migmatites that indicate protracted periods above the solidus (Finch et al., 2017; Montero et al., 2004; Rubatto et al., 2001; Weinberg et al., 2013; Williams et al., 1996) making lower crustal sections susceptible to

repeated episodes of melting and tectonically responsive (Alessio et al., 2018). This is however a simplified view, since large time-spans of crustal melting cannot be attributed to radiogenic heating alone (see discussion for the Famatinian Orogen in Wolfram et al., 2018). Moreover, increased heating may lead to extensional collapse (Vanderhaeghe, 2009) reinforcing granite production and the general higher susceptibility of radiogenic crust to high-temperature / low-pressure melting (Goffé et al., 2003).

Although anatexis of metasedimentary piles in the back-arcs of accretionary orogens can contribute to the redistribution of mass in the crust, the process is inefficient in differentiating the crust in the HPE U and Th, typically hosted by accessory minerals. The redistribution of these elements appears to require either a source that is already strongly enriched (Alessio et al., 2018; Bea, 2012), voluminous arc magmatism with significant contribution of mantle magmas and generation of new crust (Kemp and Hawkesworth, 2003) or post-orogenic A-type granites, such as the voluminous granites that intruded in the late phases of the Delamerian Orogen (Foden et al., 2002). The latter are considerably hotter than S-type magmas, and able to dissolve and transfer effectively the above elements.

CONCLUSIONS

A combination of field relationships, whole rock geochemistry and investigation of the distribution of accessory minerals from Kangaroo Island migmatitic turbidites shows that fractionation of melt in leucosomes and partitioning of Zr, Y, REE and the heat producing elements U and Th between melt and source are affected by *in source* melt crystallization due to chemical disequilibrium between migrating magma and country rock. As melt crystallizes in the source and fractionates to form a range of granitic rocks, it tracks the saturation curve of accessory minerals and becomes depleted in the trace elements that form these minerals.

Because accessory minerals crystallize preferentially in association with biotite, the biotite-rich selvedges become enriched in newly grown accessory minerals, gaining in the trace elements that form them that are lost from the melt by diffusion. This is a process that can explain multiple examples of granites that are poor in U, Th, Zr, Y and LREE, and migmatite terranes that retain or are enriched in these elements (Alessio et al., 2018). The preferential growth of monazite and zircon in the selvedge, makes the melanosomes the best place for dating. If, however melanosomes are remobilized through erosion by flowing magmas or by bulk source remobilization to form diatexites, then magmas will become enriched in these elements. We argue that the intense reworking and melting of the massive metasedimentary piles of many accretionary orogens does not necessarily lead to an upper crust rich in the heat producing elements U and Th (Alessio et al., 2018). This has been recorded extensively along the Paleozoic margin of Gondwana from SE Australia to NW Argentina. Instead, the enrichment of the upper crust in these elements takes place most effectively in other tectonic environments, such as magmatic arcs.

ACKNOWLEGEMENTS

This work was financially supported by ARC grant DP110102543. The authors acknowledge use of the facilities and the assistance of Xi-Ya Fang at the Monash Centre for Electron Microscopy. Jay Thompson from the University of Tasmania and Massimo Raveggi are thanked for their support in major and trace element analyses. We would also like to thank the careful and thoughtful comments of F. Bea and A. Kent, which strongly improved the manuscript.

List of Supporting Information

1 Lithological map as Google Earth file

2 Detailed methods of whole rock geochemical analyses

3 BSE maps of all samples with location of accessory minerals

4 Additional diagrams of accessory mineral distribution

5 Complete results of mass balance calculation

6 Raw accessory minerals dataset

References

Acosta-Vigil, A., Buick, I., Cesare, B., London, D., Morgan, G.B. (2012). The extent of equilibration between melt and residuum during regional anatexis and its implications for differentiation of the continental crust: a study of partially melted metapelitic enclaves. *Journal of Petrology* **53**, 1319-1356.

Acosta-Vigil, A., London, D., Morgan, G. (2006). Experiments on the kinetics of partial melting of a leucogranite at 200 MPa H_2O and 690–800°C: compositional variability of melts during the onset of H_2O-saturated crustal anatexis. *Contributions to Mineralogy and Petrology* **151**, 539-557.

Acosta-Vigil, A., London, D., Morgan Vi, G.B. (2005). Contrasting interactions of sodium and potassium with H_2O in haplogranitic liquids and glasses at 200 MPa from hydration–diffusion experiments. *Contributions to Mineralogy and Petrology* **149**, 276-287.

Alessio, K.L., Hand, M., Kelsey, D.E., Williams, M.A., Morrissey, L.J., Barovich, K. (2018). Conservation of deep crustal heat production. *Geology* **46**, 335-338.

Aranovich, L.Y., Makhluf, A.R., Manning, C.E., Newton, R.C. (2014). Dehydration melting and the relationship between granites and granulites. *Precambrian Research* **253**, 26-37.

Bacon, C.R, (1989). Crystallization of accessory phases in magmas by local saturation adjacent to phenocrysts. *Geochimica et Cosmochimica Acta* **53**, 1055-1066.

Bartoli, O., Acosta-Vigil, A., Ferrero, S., Cesare, B. (2016). Granitoid magmas preserved as melt inclusions in high-grade metamorphic rock. *American Mineralogist* **101**, 1543-1559.

Bea, F. (1996a). Controls on the trace element composition of crustal melts. *Transactions of the Royal Society of Edinburgh: Earth Sciences*, **87**(1-2), 33-41.

Bea, F. (1996b). Residence of REE, Y, Th and U in Granites and Crustal Protoliths; Implications for the Chemistry of Crustal Melts. *Journal of Petrology* **37**, 521-552.

Bea, F. (2012). The sources of energy for crustal melting and the geochemistry of heat-producing elements. *Lithos* **153**, 278-291.

Bea, F., Fershtater, G., Corretgé, L.G. (1992). The geochemistry of phosphorus in granite rocks and the effect of aluminium. *Lithos* **29**, 43-56.

Bea, F., Montero, P., González-Lodeiro, F., Talavera, C. (2007). Zircon inheritance reveals exceptionally fast crustal magma generation processes in Central Iberia during the Cambro-Ordovician. *Journal of Petrology* **48**, 2327-2339.

Bea, F., Pereira, M.D., Stroh, A. (1994). Mineral/leucosome trace-element partitioning in a peraluminous migmatite (a laser ablation-ICP-MS study). *Chemical Geology* **117**, 291-312.

Boehnke, P., Watson, E.B., Trail, D., Harrison, T.M., Schmitt, A.K. (2013). Zircon saturation re-revisited. *Chemical Geology* **351**, 324-334.

Brown, M. (2013). Granite: From genesis to emplacement. *Geological Society of America Bulletin* **125**, 1079-1113.

Brown, M., Rushmer, T. (2006). Evolution and differentiation of the continental crust. Cambridge University Press, Cambridge, UK.

Büttner, S.H., Glodny, J., Lucassen, F., Wemmer, K., Erdmann, S., Handler, R., Franz, G. (2005). Ordovician metamorphism and plutonism in the Sierra de Quilmes metamorphic complex: Implications for the tectonic setting of the northern Sierras Pampeanas (NW Argentina). *Lithos* **83**, 143-181.

Cawood, P.A., Kröner, A., Collins, W.J., Kusky, T.M., Mooney, W.D., Windley, B.F. (2009). Accretionary orogens through Earth history. *Geological Society, London, Special Publications* **318**, 1-36.

Clarke, G.L., White, R.W., Lui, S., Fitzherbert, J.A., Pearson, N.J. (2007). Contrasting behaviour of rare earth and major elements during partial melting in granulite facies migmatites, Wuluma Hills, Arunta Block, central Australia. *Journal of Metamorphic Geology* **25**, 1-18.

Clemens, J.D., Stevens, G. (2012). What controls chemical variation in granitic magmas? *Lithos* **134–135**, 317-329.

Clemens, J.D., Stevens, G. (2016). Melt segregation and magma interactions during crustal melting: Breaking out of the matrix. *Earth-Science Reviews* **160**, 333-349.

Finch, M.A., Weinberg, R.F., Hasalová, P., Becchio, R., Fuentes, M.G., Kennedy, A. (2017). Tectono-metamorphic evolution of a convergent back-arc: The Famatinian orogen, Sierra de Quilmes, Sierras Pampeanas, NW Argentina. *GSAB* **129**, 1602 - 1621.

Foden, J.D., Elburg, M.A., Dougherty-Page, J., Burtt, A. (2006). The timing and duration of the Delamerian orogeny: Correlation with the Ross Orogen and implications for Gondwana assembly. *Journal of Geology* **114**, 189-210.

Foden, J.D., Elburg, M.A., Turner, S.P., Sandiford, M., O'Callaghan, J., Mitchell, S. (2002). Granite production in the Delamerian Orogen, South Australia. *Journal of the Geological Society* **159**, 557-575.

Goffé, B., Bousquet, R., Henry, P., Le Pichon, X. (2003). Effect of the chemical composition of the crust on the metamorphic evolution of orogenic wedges: Effect of crustal composition on metamorphism. *Journal of Metamorphic Geology* **21**, 123-141.

Guernina, S., Sawyer, E.W. (2003). Large-scale melt-depletion in granulite terranes: an example from the Archean Ashuanipi Subprovince of Quebec. *Journal of Metamorphic Geology* **21**, 181-201.

Guevara, V.E., Caddick, M.J. (2016). Shooting at a moving target: phase equilibria modelling of high-temperature metamorphism. *Journal of Metamorphic Geology* **34**, 209-235.

Hacker, B.R., Kelemen, P.B., Behn, M.D. (2015). Continental Lower Crust. *Annual Review of Earth and Planetary Sciences* **43**, 167-205.

Haines, P.W., Turner, S.P., Foden, J.D., Jago, J.B. (2009). Isotopic and geochemical characterisation of the Cambrian Kanmantoo Group, South Australia: implications for stratigraphy and provenance. *Australian Journal of Earth Sciences* **56**, 1095-1110.

Hammerli, J., Spandler, C., Oliver, N.H.S. (2016). Element redistribution and mobility during upper crustal metamorphism of metasedimentary rocks: an example from the eastern Mount Lofty Ranges, South Australia. *Contributions to Mineralogy and Petrology* **171**, 36.

Herzberg, C., Rudnick, R. (2012). Formation of cratonic lithosphere: An integrated thermal and petrological model. *Lithos* **149**, 4-15.

Jago, J.B., Gum, J.C., Burtt, A.C., Haines, P.W. (2003). Stratigraphy of the Kanmantoo Group: A critical element of the Adelaide Fold Belt and the Palaeo-Pacific plate margin, Eastern Gondwana. *Australian Journal of Earth Sciences* **50**, 343-363.

Johannes, W., Holtz, F. (1996). Petrogenesis and experimental petrology of granitic rocks. Springer, Berlin, New York.

Johnson, T.E., White, R.W., Powell, R. (2008). Partial melting of metagreywacke: a calculated mineral equilibria study. *Journal of Metamorphic Geology* **26**, 837-853.

Kemp, A.I.S., Hawkesworth, C.J. (2003). Granitic perspectives on the generation and secular evolution of the continental crust. *Treatise on Geochemistry* **3**, 349-410.

Kriegsman, L.M., Hensen, B.J. (1998). Back reaction between restite and melt: Implications for geothermobarometry and pressure-temperature paths. *Geology* **26**, 1111-1114.

Mancktelow, N.S. (1990). The structure of the southern Adelaide Fold Belt, South Australia, in: Jago, J.B., Moore, P.S. (Eds.), The evolution of a late Precambrian-early Palaeozoic rift complex: the Adelaide geosyncline. *Geological Society of Australia; Special Publication*,. 369-395.

Milord, I., Sawyer, E.W., Brown, M. (2001). Formation of diatexite migmatite and granite magma during anatexis of semi-pelitic metasedimentary rocks: an example from St. Malo, France. *Journal of Petrology* **42**, 487-505.

Montel, J.-M. (1993). A model for monazite/melt equilibrium and application to the generation of granitic magmas. *Chemical Geology* **110**, 127-146.

Montero, P., Bea, F., Zinger, T.F., Scarrow, J.H., Molina, J.F., Whitehouse, M. (2004). 55 million years of continuous anatexis in Central Iberia: single-zircon dating of the Pena Negra Complex. *Journal of the Geological Society* **161**, 255-263.

Morgan, G.B., Acosta-Vigil, A., London, D. (2008). Diffusive equilibration between hydrous metaluminous-peraluminous haplogranite liquid couples at 200 MPa (H2O) and alkali transport in granitic liquids. *Contributions to Mineralogy and Petrology* **155**, 257-269.

Nicoli, G., Stevens, G., Moyen, J.F., Vezinet, A., Mayne, M. (2017). Insights into the complexity of crustal differentiation: K2O-poor leucosomes within metasedimentary migmatites from the Southern Marginal Zone of the Limpopo Belt, South Africa. *Journal of Metamorphic Geology* **35**, 999-1022.

Rapp, R.P., Watson, E.B. (1986). Monazite solubility and dissolution kinetics: implications for the thorium and light rare earth chemistry of felsic magmas. *Contributions to Mineralogy and Petrology* **94**, 304-316.

Rubatto, D., Williams, I.S., Buick, I.S. (2001). Zircon and monazite response to prograde metamorphism in the Reynolds Range, central Australia. *Contributions to Mineralogy and Petrology* **140**, 458-468.

Sandiford, M., McLaren, S. (2002). Tectonic feedback and the ordering of heat producing elements within the continental lithosphere. *Earth and Planetary Science Letters* **204**, 133-150.

Sawyer, E.W. (1987). The role of partial melting and fractional crystallization in determining discordant migmatite leucosome compositions. *Journal of Petrology* **28**, 445-473.

Sawyer, E.W. (1991). Disequilibrium melting and the rate of melt-residuum separation during migmatization of mafic rocks from the Grenville Front, Quebec. *Journal of Petrology* **32**, 701-738.

Sawyer, E.W. (2008). Atlas of Migmatites. NRC Research Press and Mineralogical Association of Canada.

Sawyer, E.W., Cesare, B., Brown, M. (2011). When the continental crust melts. *Elements* **7**, 229-234.

Schwindinger, M., Weinberg, R.F. (2017). A felsic MASH zone of crustal magmas — Feedback between granite magma intrusion and in situ crustal anatexis. *Lithos* **284–285**, 109-121.

Schwindinger, M., Weinberg, R.F., Clos, F. (2019). Wet or dry? The difficulty of identifying the presence of water during crustal melting. *Journal of Metamorphic Geology* **37**, 339– 358

Solar, G.S., Brown, M. (2001). Petrogenesis of migmatites in Maine, USA: Possible source of peraluminous leucogranite in plutons? *Journal of Petrology* **42**, 789-823.

Spear, F.S., Pyle, J.M. (2002). Apatite, monazite, and xenotime in metamorphic rocks. *Reviews in Mineralogy and Geochemistry* **48**, 293-335.

Stepanov, A.S., Hermann, J., Rubatto, D., Rapp, R.P. (2012). Experimental study of monazite/melt partitioning with implications for the REE, Th and U geochemistry of crustal rocks. *Chemical Geology* **300–301**, 200-220.

Tassone, D.R. (2008). Crustal melting and melt extraction: the role of migmatites in the evolution of the southern Adelaide Fold-thrust belt, Honours Thesis. The University of Adelaide, Adelaide, p. 107.

Taylor, J., Nicoli, G., Stevens, G., Frei, D., Moyen, J.F. (2014). The processes that control leucosome compositions in metasedimentary granulites: perspectives from the Southern Marginal Zone migmatites, Limpopo Belt, South Africa. Journal of Metamorphic Geology **32**, 713-742.

Taylor, S.R., McLennan, S.M. (1995). The geochemical evolution of the continental crust. *Reviews of Geophysics* **33**, 241-265.

Turner, S., Foden, J.D., Sandiford, M., Bruce, D. (1993). Sm-Nd isotopic evidence for the provenance of sediments from the Adelaide Fold Belt and southeastern Australia with implications for episodic crustal addition. *Geochimica et Cosmochimica Acta* **57**, 1837-1856.

Vanderhaeghe, O. (2009). Migmatites, granites and orogeny: Flow modes of partially-molten rocks and magmas associated with melt/solid segregation in orogenic belts. *Tectonophysics* **477**, 119-134.

Villaseca, C., Orejana, D., Paterson, B.A. (2007). Zr–LREE rich minerals in residual peraluminous granulites, another factor in the origin of low Zr–LREE granitic melts? *Lithos* **96**, 375-386.

Watson, B.E. (1988). The role of accessory minerals in granitoid geochemistry, First Hutton meeting on the origin of granites and related rocks, Vol. 1. Royal Society of Edinburgh, Edinburgh, 19-20.

Watson, E.B., Harrison, T.M. (1983). Zircon saturation revisited: temperature and composition effects in a variety of crustal magma types. *Earth and Planetary Science Letters* **64**, 295-304.

Watson, E.B., Harrison, T.M. (1984). Accessory minerals and the geochemical evolution of crustal magmatic systems: a summary and prospectus of experimental approaches. *Physics of the Earth and Planetary Interiors* **35**, 19-30.

Watson, E.B., Vicenzi, E., Rapp, R. (1989). Inclusion/host relations involving accessory minerals in high-grade metamorphic and anatectic rocks. *Contributions to Mineralogy and Petrology* **101**, 220-231.

Watt, G.R., Burns, I.M., Graham, G.A. (1996). Chemical characteristics of migmatites: accessory phase distribution and evidence for fast melt segregation rates. Contributions to Mineralogy and Petrology **125**, 100-111.

Weinberg, R.F., Becchio, R., Farias, P., Suzaño, N., Sola, A. (2018). Early paleozoic accretionary orogenies in NW Argentina: Growth of West Gondwana. *Earth-Science Reviews* **187**, 219-247.

Weinberg, R.F., Hasalová, P., Ward, L.K., Fanning, C.M. (2013). Interaction between deformation and magma extraction in migmatites: Examples from Kangaroo Island, South Australia. *Geological Society of America Bulletin* **125**, 1282-1300.

White, R.W., Powell, R. (2002). Melt loss and the preservation of granulite facies mineral assemblages. *Journal of Metamorphic Geology* **20**, 621-632.

White, R.W., Powell, R.,(2010). Retrograde melt–residue interaction and the formation of near-anhydrous leucosomes in migmatites. Journal of Metamorphic Geology **28**, 579-597.

Williams, I.S., Buick, I.S., Cartwright, I. (1996). An extended episode of early mesoproterozoic metamorphic fluid flow in the Reynolds Range, central Australia. *Journal of Metamorphic Geology* **14**, 29-47.

Wolf, M.B., London, D. (1994). Apatite dissolution into peraluminous haplogranitic melts: An experimental study of solubilities and mechanisms. *Geochimica et Cosmochimica Acta* **58**, 4127-4145.

Wolf, M.B., London, D. (1995). Incongruent dissolution of REE- and Sr-rich apatite in peraluminous granitic liquids; differential apatite, monazite, and xenotime solubilities during anatexis. *American Mineralogist* **80**, 765-775.

Wolfram, L.C., Weinberg, R.F., Hasalová, P., Becchio, R. (2018). How melt segregation impacts on granite chemistry: migmatites from the Sierra de Quilmes, NW Argentina. Journal of Petrology **58**, 2239-2364.

Yakymchuk, C., Brown, M. (2014). Consequences of open-system melting in tectonics. *Journal of the Geological Society* **171**, 21-40.

Yakymchuk, C., Brown, M. (2019). Divergent behaviour of Th and U during anatexis: Implications for the thermal evolution of orogenic crust. *Journal of Metamorphic Geology* **37**, 899-916.

List of Table Headers:

Table 1: Whole rock major and trace elements of Kangaroo Island rocks

Table 2: Distribution of accessory minerals expressed by their area. The first number is the fraction of each accessory mineral across different domains (e.g. 8.36 % of the total apatite measured is located in the leucosome) and the number in brackets is the modal percentage of the mineral in each domain. The raw data for these calculations is provided in Electronic Appendix 6. The row labelled "percentage of total" lists their proportion among all recorded minerals and is used in Fig. 6d and Fig. 11.

Table 3: LA-ICP-MS trace element analyses. Concentrations in ppm

Table 4: Modelled trace element composition of different thin section domains. The composition was calculated using the modal content from Table 2 and multiplied by the average trace element concentration of each accessory mineral in Table 3. The data is compared to the ranges of whole rock compositions in Fig. 13. A more detailed table, including the contributions of single minerals is provided in Electronic Appendix 5.

List of Figure Captions:

Figure 1

Location of Kangaroo Island within the Adelaide fold belt, highlighting the position of the migmatites in the field area (black rectangle) and the position of Delamerian granite intrusions (modified after Schwindinger & Weinberg, 2017).

Figure 2

Common lithologies at the south coast of Kangaroo Island. **(a)** Metatexite migmatite showing interlayered psammites and pelites. Lower part of the photograph shows two leucosomes along the same plane with poorly developed mafic selvedges and communicating with one another, linked by discontinuous small in situ leucosome patches (white arrows). Pelite layers have more leucosomes than psammite suggesting they were more fertile during anatexis. The top of the photograph shows a folded leucosome with narrow melanosome (black arrow). The white boxes mark locations of samples 6ML1_1 and 6ML1_6 used for the thin sections and BSE maps used in Figures 2 and 5. **(b)** Diatexite migmatite characterized by a heterogeneous magmatic matrix with leucocratic (white arrow) and mesocratic (black arrow) domains. Psammite schollen of different sizes, schlieren and biotite-clots illustrate variable degrees of metatexite disaggregation. White box indicates the position of sample 6ML21_1 used for the thin section shown in Fig. 3d. **(c)** Intrusive granite (top) in irregular, curved contact with heterogeneous diatexite (bottom). Note coarse grain size, presence of K-feldspar megacrysts and a more leucocratic nature of the granite. **(d)** Dark grey, biotite-bearing tonalitic dike concordantly intruding a 300m wide leucogranite body, assembled by multiple single sheets. Lobate, diffuse contacts between both and the presence of irregular leucogranite pillows in the dike (arrows) indicate both are co-magmatic and mingled.

Figure 3

Photomicrographs of leucosome types in metatexite and diatexite. **(a)** Ptygmatically folded leucosome in sample 6ML1_1 (see Fig. 2a for location), contrasts with the surrounding mesosome by coarser average grain size, leucocratic appearance and strongly developed mafic selvedge that is partly enclosed in between fold hinges and entrained into leucosome. The leucosome has tonalitic composition, comprised of quartz, plagioclase and minor biotite. **(b)** Detail of (a) showing coarse biotite in selvedge with abundant inclusions of accessory mineral (apatite, monazite, xenotime, zircon), indicated by pleochroic halos (arrows). **(c)** Metatexite sample 6ML1_6 comprising a pelitic layer (PL) and a psammite layer (PS) with several leucosomes (L). In contrast to sample 6ML1_1, a selvedge is only weakly developed and domains are less clearly defined. **(d)** Diatexite sample 6ML21_1 rich in biotite (see Fig. 2b for location). Some of the biotite is likely inherited from the source, suggested by *in situ* disaggregation of metatexite in the formation of diatexite magma (Fig. 2b).

Figure 4

Evolution of a granitic transport and fractionation system from source to sink in the scale of meters. Photographs a-c show different aspects of a single connected networks and (d) shows a sketch of a granite network where the host rock changes from psammo-pelite to psammite and the composition within the granite changes from tonalite to granite to quartz segregations. **(a)** In the root zone, centimetric tonalitic leucosome in a psammo-pellitic layer merge to form continuous, stromatic leucosomes. **(b)** Individual leucosomes merge into coarser grained granite veins crosscutting the host rock at high angles to its foliation. **(c)** At the end of this continuous vein network, the coarse-grained granite veins are directly linked to thin quartz veinlets. **(d)** Schematic representation the studied melt transport and fractionation system where leucosomes represent the pathways of melts extracted from the root zone. These traverse a lithological contact between a migmatitic pelite and intrudes into psammite as a sharp planar dyke that dies out as quartz veins.

Figure 5

Photomicrographs recording the fractionation across the different sections of the network in Fig. 4. **(a)** Root zone: leucosome in the centre of the image consists of plagioclase and quartz with several enclosed biotite grains and diffuse margins to the surrounding finer-grained psammo-pelite. **(b)** Detail of the continuous stromatic leucosomes in Fig. 4a, showing the network of touching plagioclase grains and interstitial quartz. **(c)** Zone of merging leucosomes into veins of coarse-grained granite (Fig. 4b) and first appearance of K-feldspar (microcline). **(d)** Planar dike in psammite: coarse-grained granite in the centre with sharp general contact with psammite, serrated at grain scale.

Figure 6

BSE map of folded leucosome sample 6ML1_1 (see Fig. 2 for location) showing all detected accessory minerals. **(a)** BSE map of entire thin section compiled of >200 single frames. **(b)** Magnification of marked area in (a) showing apatite in red, monazite in blue, zircon in purple and xenotime in green. Except apatite, most accessory minerals in this thin section, are <100 μm and either included in or located at the grain boundaries of biotite. **(c)** BSE map showing location of all detected accessory minerals. Dots correspond to position of different minerals and do not represent grain size. Coloured background shows division into leucosome, selvedge and mesosome. Note the sparse accessory mineral abundance in leucosome. **(d)** Bar plot on left shows the modal proportion of accessory minerals in each domain (area covered by accessory minerals divided by total area of domain). The modal abundance of accessories minerals in the selvedge (0.129) is nearly 20x that in leucosome (0.006) or 4x that in mesosome (0.031). Apatite is excluded, because its large modal proportion does not allow to show all accessory minerals in a single bar plot, but the same distribution relationships across the domains is maintained (see Electronic Appendix 4). The column on the right shows distribution of accessory minerals and their modal proportion in the entire thin section. Apatite comprises 80 % of the total accessories measured by area, which is 0.15 modal % of sample 6ML1_1. Percentage values below x-axis indicate the total area of each domain in this thin section.

Figure 7

Size distribution for zircon grains across different domains. The majority of grains across all domains have grain sizes <30µm. Larger grains between 80-100µm are in the mafic selvedge and to a smaller extent in the mesosomes.

Figure 8

Bivariate major element plots for magmatic and metasedimentary rocks: **(a)** ASI (molar $Al_2O_3/(CaO + Na_2O + K_2O)$ vs. SiO_2 ; **(b)** $MgO+FeO_T$ vs. SiO_2 ; and **(c)** $MgO+FeO_T$ vs. K_2O. Grey background defines the field occupied by low-grade, unmelted Kanmantoo Group rocks, the likely source for the magmatic rocks (data from Haines et al., 2009; Turner et al., 1993). The two samples of protolith analysed here are indicated by crosses. In (b) the main trend bifurcates at 74 % SiO_2 indicating two different magmatic processes in the petrogenesis of the granitoids (adapted after Foden et al., 2002). (c) Plot of melt incompatible ($MgO + FeO_T$) vs. compatible elements (K_2O) with vectors pointing towards residual garnet, cordierite, muscovite, plagioclase and biotite (after Milord et al., 2001). At the base of the plot, felsic granitoids define a subhorizontal fractionation trend with tonalitic compositions at low K_2O, and K-feldspar-rich leucogranites at high K_2O. Diatexites and intrusive granites follow a negative diagonal trend from the centre of the Kanmantoo Group, reflecting different degrees of separation of melt from source material (melt-residuum separation), and mixing between anatectic and intrusive magmas (described in Schwindinger and Weinberg, 2017 and Foden et al., 2002). Biotite-rich schlieren and residual layers plot parallel to the biotite vector, indicating their residual nature. Smaller and transparent symbols represent samples from Foden et al. (2002) and Tassone (2008).

Figure 9

Chondrite-normalized REE plots (McDonough and Sun, 1995). Grey background marks the field defined by two samples of Kanmantoo Group protolith analysed in this study. **(a)** Diatexite, residual layers and intrusive granites match the REE composition of the source, while psammite-rich diatexites are slightly poorer. **(b)** Strong REE variation among the felsic granitoids and tonalite dikes. Leucosomes and leucogranites are depleted in LREE, but have a weakly positive HREE trend, causing some samples to have concentrations above the Kanmantoo Group. Tonalite dikes are strongly enriched in HREE. The small coloured squares on the right indicate K_2O content and show that tonalite samples, with lowest K_2O contents, are most enriched in REE.

Figure 10

Bivariate trace element plots: (a) Zr, (b) Th, (c,d) ∑LREE, (e) U vs. $MgO+FeO_T$ and (f) Y vs. ∑HREE. $MgO+FeO_T$ on the x-axes of the plots is strongly associated with the modal proportion of biotite in the rocks, since biotite in the only major mineral that contain FeO + MgO. **(a-c)** Light blue horizontal line shows average concentrations of the upper continental crust (UCC, Rudnick and Gao, 2014). The vertical dashed line divides the diagram into two: for higher values of $MgO+FeO_T$ diatexite and granite samples define a plateau close to or slightly above the field for the Kanmantoo group. For lower values all three diagrams show that felsic granitoids are impoverished in the trace element, with values below saturation calculated for different temperatures (red dashed lines). Zircon saturation values were calculated after Boehnke et al. (2013) at M-value = 1.2 (average of the magmatic rocks, Table 1), and LREE-equilibrium concentration were calculated using the equation of Stepanov et al. (2012) with 5 wt.% H_2O. **(d)** For comparison with (c), higher temperature anatectic turbidites from the Puncoviscana Formation, Sierra de Quilmes and Sierra de Molinos in NW Argentina define similar trends as in (c) with a sharp drop in ΣLREE for the felsic granitoids (from Wolfram et al., 2018). **(e)** U has no clear correlation with $MgO+FeO_T$ and has similar values to the Kanmantoo Group, except for the tonalite dikes that are enriched in U. **(f)** Strong correlation between Y vs. ∑HREE (R^2= 0.992), suggest that they are both hosted by the same mineral, most likely

xenotime. Inset shows magnified ternary plot of U, Y and ∑HREE. Except for leucogranites, which are offset to higher U possibly by the existence of another U-hosting minerals, all rocks have the same ratio confirming the control of xenotime on these elements. See Figure 7 for legend.

Figure 11

Location of accessory minerals in sample 6ML1_1. Apatite has large grainsizes, is usually located at grain boundaries and therefore excluded from the plot **(a)** BSE image of a small section of sample 6ML1_1 indicating inclusions of accessory minerals in or at the edge of biotite, quartz, plagioclase, muscovite. **(b)** Bar plot summarizing the location of all accessory minerals in leucosome, selvedge or mesosome. The total number of counted grains increases from leucosome to mesosome, with the bulk of accessory minerals being included or located at the edge of biotite. The biotite-rich selvedge has the highest proportion of accessory mineral inclusion in biotite, and ~40 % of accessory minerals in the mesosome are located either inside plagioclase or quartz. Colours match the grain type and position marked in (a).

Figure 12

Results of LA-ICP-MS and EDS elemental analyses. **(a)** U/Th vs ΣREE for zircon and apatite grains across different domains suggests no systematic correlation between position of minerals and their composition. Apatite plots at a higher U/Th ratio than zircon, because of its very low Th contents (see Table 3). **(b)** Distribution of trace elements in different accessory minerals in sample 6ML1_1. Zircon is the only host of zirconium. Monazite controls distribution of LREE. U is distributed over multiple minerals with monazite having the largest fraction. HREE have been excluded due to insufficient analyses.

Figure 13

Calculated composition of the three domains in 6ML1_1 using data in Tables 2 and 3 for mineral composition and modal content, compared to the ranges of whole rock geochemistry of natural samples (data in Table 4). Even though the data is based on only a 2 x 3 cm thin section, there is good agreement for most elements. For Zr, ΣLREE and Th, the leucosome (L) plots at the low end of the felsic granitoid range, the mesosome (M) plots within psammitic diatexite range and the selvedge (S) plots at the higher end or above the range defined by residual lithologies and magmas rich in source rafts and schlieren. Y and ΣHREE tend to be underestimated most likely because of the neglect of xenotime (Fig. 10f).

Figure 14:

Bivariate trace element plots of bulk rock samples analysed as well as compositions derived from mass balance calculations for different domains in migmatite samples 6ML1_1, 6ML1_6 and diatexite sample 6ML21_1 shown by the coloured circles connected by a dashed line. **(a)** Positive correlation between Zr and ΣLREE (hosted by zircon and monazite, respectively) in bulk rock composition is matched by calculated domain compositions for sample 6ML1_1, while domains in 6ML1_6 or the diatexite sample 6ML21_1 have lower ΣLREE. For 6ML1_1, leucosomes coincide with the most depleted felsic granitoids, the mesosomes with anatectic psammites, and the selvedge plots outside the figure limits at Zr = 355ppm, but within typical ΣLREE of granites and residual rocks at 188 ppm. **(b)** Calculated values of all samples agree well with natural samples for Th vs. U. Leucogranites have higher U when compared to the trend defined by the calculated values for the three domains, which possibly relates to the presence of other U-minerals (e.g. uraninite). **(c, d)** Th vs. P_2O_5 where (d) shows Y as a third variable indicated by the colour of the points. They show three different trends starting from a point that would reflect a slightly impoverished initial melt. The red arrow includes the fractionated felsic granitoids and show enrichment in P_2O_5 without gaining either Th or Y indicative of Apatite enrichment. A subvertical trend at low P_2O_5 towards high Th and Y (blue arrow) and

defined by one tonalitic leucosome, a diatexite and the tonalite dikes, indicate higher modes of xenotime (Y) and monazite (Th), possibly representing remobilized cumulates. A diagonal trend (green arrow) including rocks rich in residual material represents different degrees of source contamination, containing accessory minerals in quantities dictated by the Kanmantoo Group protolith and the efficiency of filtering.

Table 1. Whole rock major and trace elements of Kangaroo Island rocks

Lithology	**Protolith**		**Leucosome**				**Anatectic psammite**	**Residual layers**			**Psammite-rich Diatexite**				**Diatexite**	
Sample	HR1	PS 1	6ML9_2	SSBR 22	VB26-3	VB6_2	VB26-2	6ML1a_1	6ML1a_2	VB26_9	SSBR 24	SSBR 5	VB30_1	SSBR 12	6ML-21-1	VB27-1
comment			Pl-rich		Kfs-rich	Kfs-rich		Bt-rich	Bt-rich	Bt-rich	Qtz-rich	Qtz-rich	Qtz-rich	Qtz-rich	Bt-rich	Bt-rich
Major elements [wt. %]																
SiO_2	68.93	62.95	76.39	74.77	74.97	74.48	79.55	66.17	56.21	55.38	78.44	78.73	78.57	79.02	69.75	69.30
TiO_2	0.63	0.75	0.18	0.14	0.12	0.09	0.22	0.73	0.82	1.27	0.16	0.30	0.23	0.22	0.49	0.55
Al_2O_3	13.30	16.30	12.92	13.60	13.09	13.19	10.55	14.52	19.33	15.30	11.19	10.42	10.68	10.26	14.02	14.14
FeO_T	5.44	6.08	1.26	0.97	0.84	0.80	1.72	5.51	7.28	11.43	1.06	1.87	1.54	1.44	3.69	3.99
MnO	0.07	0.10	0.02	0.01	BLD			0.08	0.13	0.14	0.01	0.03	0.01	0.02	0.06	0.07
MgO	2.43	3.44	0.74	0.57	0.38	0.23	0.71	3.04	4.38	5.06	0.52	0.83	0.71	0.70	2.08	2.18
CaO	1.94	2.27	1.91	1.49	0.38	0.31	0.58	1.83	0.83	0.28	1.04	1.33	0.41	0.89	1.79	1.94
Na_2O	2.31	1.99	2.53	2.78	2.35	2.92	3.15	2.13	1.04	1.23	2.21	2.40	2.89	1.69	2.36	2.58
K_2O	2.93	3.76	2.81	4.55	6.51	6.26	2.41	3.72	6.22	6.45	4.37	2.68	3.33	4.03	3.34	3.29
P_2O_5	0.11	0.15	0.05	0.09	0.09	0.25	0.09	0.17	0.15	0.09	0.04	0.10	0.14	0.11	0.14	0.06
BaO	0.06	0.08	0.07	0.12	0.19	0.15	0.07	0.08	0.19	0.15	0.12	0.07	0.07	0.08	0.07	0.05
LOI	0.88	1.64	0.74	0.82	0.57	0.78	0.55	1.09	2.38	1.57	0.64	0.77	0.86	1.13	1.28	0.77
Total	99.63	100.19	99.75	100.02	99.59	99.55	99.79	99.70	99.76	99.63	99.92	99.74	99.61	99.76	99.49	99.36
ASI[a]	1.27	1.42	1.21	1.11	1.13	1.09	1.19	1.34	1.94	1.61	1.09	1.12	1.17	1.17	1.30	1.25
Trace elements [ppm]																
V	76.54	74.67	18.23	14.12	9.85	12.14	27.36	90.11	131.60	133.99	15.69	22.44	23.25	16.55	44.50	76.70
Zn	82.58	28.18	27.58	14.75	10.00	8.20	15.15	89.87	114.66	126.29	12.58	23.94	14.62	20.82	56.88	61.18
Rb	142.73	175.15	93.94	118.33	152.07	149.03	78.40	224.93	289.62	484.91	119.00	70.52	105.54	137.24	123.81	191.50
Sr	194.40	98.94	215.30	244.09	163.24	157.61	153.55	148.00	140.90	78.05	224.72	158.52	147.00	133.89	163.45	146.84
Y	21.69	41.66	58.85	40.94	53.65	13.56	14.75	22.00	27.03	42.84	9.68	16.19	15.47	31.90	26.94	48.00
Zr	111.58	210.65	66.14	88.93	51.20	47.71	84.54	198.53	128.74	160.85	102.12	92.26	135.67	105.37	120.44	188.79
Nb	13.07	16.90	4.13	3.77	2.98	1.40	3.87	16.32	18.21	31.83	3.29	4.20	1.90	5.11	8.94	16.79
Cs	6.43	3.17	2.75	3.43	3.16	1.36	1.22	14.10	14.57	16.64	3.25	2.49	1.60	6.45	11.66	12.70
Ba	587.33	702.88	697.18	1073.27	1643.77	1407.26	651.91	753.43	1746.52	1493.26	1134.68	603.46	699.02	753.78	611.14	479.89
Hf	3.07	5.15	2.66	2.60	1.77	1.49	2.31	5.46	3.57	4.33	2.19	2.60	3.65	3.25	3.55	5.56
La	26.56	45.62	14.97	16.99	15.60	10.05	25.44	44.09	46.22	55.60	14.36	28.30	25.87	22.90	30.63	44.66
Ce	54.15	92.08	30.05	35.65	32.52	22.00	51.04	89.19	92.31	112.90	27.90	57.99	54.91	46.46	64.37	92.71
Pr	6.33	10.40	3.65	4.01	3.82	2.32	5.62	10.46	10.87	12.13	3.15	6.53	5.94	5.27	7.19	10.74
Nd	23.11	37.58	13.24	14.40	14.11	8.42	20.05	37.75	38.95	43.21	11.08	23.66	20.98	19.01	26.02	38.85
Sm	4.43	7.54	3.21	3.41	3.70	1.83	3.80	6.89	7.24	7.82	2.17	4.44	4.03	4.07	5.26	8.59
Eu	1.09	1.13	1.55	1.06	0.89	0.79	0.86	1.38	1.45	1.61	0.88	0.95	0.96	0.99	1.15	1.25
Gd	4.42	7.32	4.37	3.71	4.23	1.75	3.18	6.33	6.85	7.99	1.85	3.87	3.22	4.02	4.52	7.31
Tb	0.68	1.14	1.01	0.77	0.99	0.31	0.48	0.89	1.00	1.22	0.28	0.56	0.49	0.71	0.75	1.23
Dy	3.83	6.63	7.59	5.46	7.38	2.01	2.65	4.52	5.23	6.91	1.58	2.99	2.77	4.56	4.51	7.43
Ho	0.79	1.34	1.93	1.28	1.84	0.46	0.54	0.83	1.00	1.46	0.31	0.56	0.58	1.00	0.99	1.64
Er	2.08	3.82	6.08	4.16	5.87	1.32	1.41	1.99	2.52	3.89	0.91	1.53	1.54	3.06	2.79	4.64
Tm	0.28	0.55	0.99	0.66	0.99	0.20	0.19	0.26	0.33	0.53	0.15	0.22	0.21	0.48	0.41	0.72
Yb	1.80	3.43	7.23	4.39	7.42	1.36	1.19	1.60	2.09	3.44	1.06	1.35	1.43	3.15	2.83	5.07
Lu	0.27	0.50	1.12	0.65	1.15	0.21	0.18	0.24	0.31	0.51	0.16	0.20	0.22	0.46	0.43	0.78
Th	9.76	23.71	10.24	11.29	11.49	3.47	7.48	18.81	20.41	15.91	5.75	10.52	9.11	11.34	12.24	21.00
U	1.72	4.76	5.33	2.95	3.56	1.19	1.52	3.50	3.97	3.88	1.07	1.61	1.66	2.11	3.75	6.54
Eu/Eu*	0.75	0.46	1.26	0.91	0.69	1.35	0.75	0.64	0.63	0.62	1.34	0.70	0.81	0.75	0.72	0.48
Zr-saturation (Boehnke et al. 2013)																
T_{Zr} [°C]	728	798	684	697	650	639	710	790	771	770	715	711	754	731	741	780
M	1.19	1.16	1.13	1.27	1.24	1.30	1.10	1.18	0.95	1.15	1.22	1.17	1.13	1.11	1.14	1.21

a) ASI: mol. Al_2O_3 / ($CaO+Na_2O+K_2O$)

Table 1 (continued)

Lithology	**Leucogranites**							**Granite**							**Tonalite**	
Sample	6ML-22-9	VB2-1	VB28-1	VB9-1	VB10-1	VB10-2	SSBR 23	6ML-22-7	6ML27_2	SSBR 10	VB20-3	VB23-1	6ML22_16	6ML22_6	VB10_14	VB10-4
comment					Grt	Grt	Bt-LG									
Major elements [wt. %]																
SiO_2	75.55	73.76	74.18	76.35	74.51	74.29	73.31	73.96	69.36	72.23	72.17	72.15	71.89	71.64	76.21	77.83
TiO_2	0.07	0.09	0.01	0.02	0.04	0.04	0.27	0.34	0.40	0.58	0.55	0.54	0.46	0.57	0.29	0.33
Al_2O_3	13.37	13.92	14.25	13.00	14.25	13.94	13.32	12.47	15.15	13.03	12.70	12.82	13.23	13.00	12.57	10.96
FeO_T	0.49	0.80	0.25	0.13	0.18	0.78	1.71	2.21	3.14	3.47	3.10	3.15	3.05	3.69	2.03	2.26
MnO						0.05	0.02	0.03	0.06	0.06	0.05	0.04	0.05	0.06	0.03	0.04
MgO	0.29	0.27	0.18	0.12	0.10	0.15	0.81	1.04	1.75	1.35	1.32	1.43	1.38	1.55	0.99	0.95
CaO	0.79	0.27	0.55	0.97	0.80	0.47	1.11	1.38	2.02	1.89	1.71	1.59	1.40	1.61	2.15	1.11
Na_2O	2.03	3.05	1.88	2.60	3.97	3.69	2.21	2.37	2.78	2.59	2.55	2.58	2.45	2.49	3.31	2.42
K_2O	6.29	6.37	6.98	5.27	4.55	4.65	5.55	4.12	3.62	3.65	3.81	3.80	4.51	3.86	1.25	2.66
P_2O_5	0.06	0.23	0.17	0.11	0.25	0.30	0.18	0.14	0.08	0.19	0.19	0.25	0.15	0.19	0.06	0.06
BaO	0.11	0.06	0.07	0.09	0.02		0.10	0.07	0.08	0.05	0.06	0.05	0.06	0.06	0.01	0.06
LOI	0.70	0.66	0.69	0.48	0.93	0.60	0.81	0.92	0.86	0.85	0.67	0.75	0.84	0.72	0.71	0.71
Total	99.81	99.58	99.23	99.17	99.61	99.05	99.59	99.32	99.65	100.34	99.22	99.49	99.80	99.85	99.83	99.64
ASI[a]	1.15	1.12	1.22	1.11	1.10	1.17	1.14	1.15	1.25	1.12	1.11	1.14	1.15	1.16	1.18	1.23
Trace elements [ppm]																
V	7.50	1.18	0.49	0.71	BD	0.87	19.97	36.88	48.99	62.13	53.17	52.27	56.10	36.88	32.30	33.54
Zn	9.51	12.98	3.92	2.69	1.17	6.99	28.79	33.41	52.42	47.53	47.86	45.51	44.53	33.41	32.37	35.39
Rb	175.44	211.58	205.86	146.45	181.07	266.40	170.57	180.64	190.01	180.30	200.42	218.06	184.99	180.64	83.65	163.27
Sr	176.33	125.52	130.16	167.72	21.38	16.16	197.25	162.94	172.70	142.72	160.65	139.33	139.21	162.94	143.70	115.04
Y	19.04	18.50	26.13	8.52	3.38	8.91	19.83	25.23	32.79	26.46	34.35	28.73	33.89	25.23	231.03	99.16
Zr	22.33	42.66	29.36	24.66	24.46	15.58	188.92	168.21	109.16	241.36	221.58	155.40	212.32	168.21	174.97	155.26
Nb	2.42	7.57	1.66	0.61	1.28	7.28	6.83	5.83	12.02	11.35	15.32	18.30	12.37	5.83	1.76	9.35
Cs	3.59	9.30	8.11	4.49	3.49	6.63	5.55	5.48	10.44	9.93	8.39	8.37	10.36	5.48	3.74	6.24
Ba	968.57	507.52	599.95	833.33	108.39	20.97	933.77	673.16	746.08	512.15	571.28	510.62	514.30	673.16	93.18	529.10
Hf	1.28	1.73	1.30	1.12	1.15	1.03	4.27	4.90	3.40	6.46	6.14	4.63	5.92	4.90	6.05	4.78
La	7.18	5.41	10.85	3.26	1.71	2.71	38.45	32.76	30.30	35.95	47.57	41.25	35.51	32.76	41.11	34.47
Ce	12.92	11.67	22.79	5.85	1.37	5.84	79.49	69.35	60.73	74.55	99.06	86.40	75.55	69.35	86.31	72.69
Pr	1.53	1.32	2.65	0.62	0.45	0.69	8.93	7.94	7.19	8.30	11.47	9.58	8.62	7.94	10.38	8.56
Nd	5.58	4.35	9.60	2.14	1.59	2.46	31.59	28.89	25.70	29.76	41.12	34.43	31.47	28.89	40.05	31.52
Sm	1.43	1.38	2.40	0.56	0.45	0.81	6.87	6.32	5.06	6.15	8.41	7.09	6.53	6.32	11.87	7.78
Eu	1.23	0.66	1.09	1.30	0.12	0.08	1.40	1.21	1.38	1.16	1.26	1.07	1.04	1.21	1.32	1.04
Gd	1.61	1.48	2.44	0.68	0.39	0.84	5.82	5.19	5.03	5.15	7.18	6.04	5.60	5.19	15.42	8.42
Tb	0.36	0.38	0.53	0.16	0.09	0.21	0.80	0.85	0.86	0.87	1.09	0.96	0.93	0.85	3.77	1.78
Dy	2.63	2.71	3.75	1.14	0.64	1.42	3.79	4.67	5.25	4.95	5.97	5.30	5.66	4.67	28.88	12.93
Ho	0.63	0.60	0.88	0.28	0.13	0.29	0.65	0.95	1.14	1.00	1.24	1.05	1.23	0.95	7.78	3.30
Er	1.95	1.74	2.70	0.85	0.37	0.83	1.72	2.45	3.29	2.55	3.23	2.72	3.41	2.45	24.75	10.32
Tm	0.33	0.27	0.45	0.14	0.06	0.14	0.25	0.35	0.52	0.37	0.44	0.36	0.51	0.35	3.98	1.59
Yb	2.47	1.91	3.33	1.04	0.48	1.01	1.64	2.45	3.81	2.59	2.82	2.25	3.58	2.45	28.37	11.19
Lu	0.39	0.27	0.51	0.16	0.07	0.14	0.25	0.37	0.59	0.37	0.41	0.33	0.54	0.37	4.36	1.68
Th	2.21	3.11	4.49	1.04	0.66	1.21	18.81	16.50	15.70	15.33	23.55	18.54	15.94	16.50	30.57	25.21
U	5.03	5.52	4.26	1.53	1.09	4.00	3.86	2.41	4.11	1.63	2.32	3.17	2.48	2.41	16.33	7.47
Eu/Eu*	2.47	1.41	1.37	6.42	0.87	0.30	0.67	0.64	0.83	0.63	0.49	0.50	0.63	0.52	0.30	0.39
Zr-saturation (Boehnke et al. 2013)																
T_{Zr} [°C]	589	632	614	593	588	562	775	766	722	796	786	752	732	787	776	775
M	1.21	1.28	1.15	1.24	1.29	1.22	1.25	1.22	1.21	1.30	1.30	1.27	1.26	1.26	1.17	1.08

a) ASI: mol. Al_2O_3 / ($CaO+Na_2O+K_2O$

Table 2: Distribution of accessory minerals expressed by their area. The first number is the fraction of each accessory mineral across different domains (e.g. 8.36 % of the total apatite measured is located in the leucosome) and the number in brackets is the modal percentage of the mineral in each domain. The raw data for these calculations is provided in Electronic Appendix 6. The row labelled "percentage of total" lists their proportion among all recorded minerals and is used in Fig. 6d and Fig. 11.

	Mineral mode across domains [area %]				Total modal	**location (without apatite)**					
Domain	Apatite	Monazite	Xenotime	Zircon	content	Bt	Bt-edge	Pl	Qtz	Ms	Kfs
6ML1_6 *(total area 592.38 mm²)*						**6ML1_6**					
Leucosome *(97.95 mm²)*	8.36 (0.057)	13.96 (0.019)	15.31 (0.003)	9.71 (0.012)		15	13	121	34	-	-
Selvedge *(88.69 mm²)*	12.27 (0.092)	16.89 (0.025)	19.34 (0.005)	19.42 (0.027)		108	28	59	10	-	-
Mesosome *(405.74 mm²)*	79.37 (0.260)	69.15 (0.046)	65.35 (0.007)	70.87 (0.043)		259	154	258	112	-	-
Total modal proportions	0.115	0.023	0.004	0.021	0.163	-	-	-	-	-	-
Percentage of total	**70.55**	**14.11**	**2.45**	**12.88**							
6ML1_1 *(total area 680.94 mm2)*						**6ML1_1** *(n = 1012)*					
Leucosome *(331.91 mm²)*	15.97 (0.053)	12.78 (0.003)	12.79 (0.0004)	8.38 (0.003)		42	41	26	3	4	-
Selvedge *(83.01 mm²)*	46.18 (0.608)	37.75 (0.035)	51.14 (0.006)	38.75 (0.088)		257	81	7	22	7	-
Mesosome *(266.02 mm²)*	37.85 (0.156)	49.47 (0.014)	36.07 (0.001)	38.75 (0.02)		142	186	93	96	5	-
Total modal proportions	0.147	0.012	0.002	0.021	0.182	441	308	126	121	16	-
Percentage of total accessory minerals	**80.77**	**6.59**	**1.10**	**11.54**							
6ML21_1 *(total area: 500.07 mm²)*						**6ML21_1** *(n = 548)*					
Diatexite	76.27 (0.138)	9.64 (0.017)	1.27 (0.002)	12.82 (0.023)		229	154	91	52	22	17

* Accessory mineral location was investigated along three representative areas of the thin section

Table 3: LA-ICP-MS trace element analyses. Concentrations in ppm

Mineral	Apatite	Apatite	Apatite	Apatite	Apatite	Apatite	Apatite	Apatite	Apatite	Apatite	Apatite	Apatite	**Mean**
Sample	6ML1_1	6ML1_1	6ML1_1	6ML1_1	6ML1_1	6ML1_1	6ML1_6	6ML1_6	6ML1_6	6ML1_6	6ML21_1	6ML21_1	
Domain	S	L	L	S	MS	MS	L	S	L	MS	D	D	
Y	1340	1241	1255	1097	1151	1929	1216	698	1268	1017	1250	1145	**1217.3**
Zr													
La	121.5	94.8	99.5	96.4	98.6	188.3	101.8	50.5	97.3	90.4	110.5	97.4	
Ce	406.5	331.2	339.7	332	343	612	348	191.6	348.1	312.3	373	332.8	
Pr	68.1	59.5	60.6	57.1	59.9	105	59.1	36	63	53.5	63	58.1	**∑LREE 1041.4**
Nd	392	347	345.1	327	358	598	346.2	221.4	362	312	360.6	337.3	
Sm	172.8	154.6	155.8	149	157.1	269	150.9	104.5	165.2	139.2	157.8	153.6	
Eu	11.89	10.7	10.98	10.5	11.67	20.74	10.27	9.03	9.39	9.07	11.37	11.94	
Gd	236.4	217.6	222.7	204.7	219.9	360	223.2	153.7	226	196.5	217.7	210.6	
Tb	47.31	42.6	44.4	40.7	43.4	71.5	43.47	29.74	44.7	38.7	43.5	41.21	
Dy	295.5	268.3	275.6	249.6	267.1	448	272.4	176.8	284.1	238.8	270.6	258.4	
Ho	55.6	51.4	52.5	45.8	48.4	82.4	51.4	30.2	53.3	44	50.7	45.8	**∑HREE 846.9**
Er	135.7	126.8	127.4	107.2	116.7	198.1	122.6	67.2	128.2	104.5	127.8	112.5	
Tm	18.22	16.49	16.43	14.01	14.79	25.92	15.87	8.5	16.57	13.07	17.71	15.55	
Yb	112.5	101.5	106.4	89.5	93	163.2	95.3	50	99.8	78.2	118.1	99.3	
Lu	14.23	12.85	13.03	11.08	11.63	19.62	11.82	6.28	12.5	10.06	15.24	12.39	
Th	1.67	0.63	1.17	0.66	1.66	17.5	1.37	0.46	1.46	0.78	0.65	0.78	**2.4**
U	83.5	57.4	71.9	54.4	75.6	262	36.7	13.9	49.4	37.7	76.1	46.9	**72.1**

Mineral	Zircon	Zircon	Zircon	Zircon	Zircon	Zircon	Zircon	Zircon	**Mean**	Monazite*	Monazite*	Monazite*	Xenotime*	Xenotime*	Xenotime*
Sample	6ML1_1	6ML1_1	6ML1_1	6ML1_1	6ML1_1	6ML1_1	6ML1_6	6ML21_1		6ML1_6	6ML1_1	6ML21_1	6ML1_6	6ML1_1	6ML21_1
Domain	S	S	S	S	MS	S	MS	D		all	all	D			
Y	750	633	659	704	331	2520	1050	657	**913.0**	3.74	3.74	3.74	31.33 *(84)*	39.99 *(51)*	44.28 (37)
Zr (%)	41.0	40.4	40.0	40.5	41.1	40.3	33.8	41	**39.8**	-			-	-	-
La	0.66	4	0.037	1.35	1.28	13.7	11.1	NA		10.35 *(898)*	14.29 *(434)*	15.17 *(190)*	-	-	-
Ce	19.4	42.5	19.78	17.2	37.8	91	46	17.1		20.17 *(999)*	*27.04 (442)*	27.85 *(220)*	-	-	-
Pr	0.62	3.19	0.123	1.4	1.76	14.5	8.2	0.043	**∑LREE 86.5**				-	-	-
Nd	4.8	20.2	1.93	11.8	14.7	98	54	0.92		8.75 *(598)*	10.19 *(414)*	12.43 *(112)*	-	-	-
Sm	5.1	11.9	3.47	11.6	9	57	28.2	2.29		-	-	-	-	-	-
Eu	1.36	2.32	0.74	3.95	3.4	15.3	9	0.21		-	-	-	-	-	-
Gd	19.3	27.5	16.4	25.7	22.8	115	57	12.8		-	-	-	-	-	-
Tb	5.8	7.8	5.15	7.4	4.8	30.9	14.8	4.62		-	-	-	-	-	-
Dy	65	72	57.6	74.4	45	289	123	56.9		-	-	-	4.41 *(11)*	4.41 *(11)*	4.41 *(11)*
Ho	24	22.3	21.6	24.8	11.9	88.5	33.6	21.8	**∑HREE 638.3**	-	-	-	-	-	-
Er	107	85.9	96.3	125.3	44	347	113	98.4		-	-	-	-	-	-
Tm	22.8	16.7	20.3	35.2	8.7	69.2	23.6	20.3		-	-	-	-	-	-
Yb	212	144	188	428	78	600	210	184		-	-	-	4.94 *(11)*	4.94 *(11)*	4.94 *(11)*
Lu	45	27.4	38	102.4	14.9	113.8	41.4	36.5		-	-	-	-	-	-
Th	153	207	187	87.8	200	221	155	74.6	**160.7**	4.59 *(59)*	5.78 *(39)*	7.89 *(8)*	1.39 *(15)*	1.39 *(15)*	1.39 *(15)*
U	143	438	343.3	663	215	579	1270	102.4	**469.2**	*1.46 (4)*	*1.46 (4)*	*1.46 (4)*	2.14 *(15)*	2.14 *(15)*	2.14 *(15)*

L = Leucosome; S= Selvedge; MS= Mesosome; D = Diatexite. *Monazite and xenotime data are average concentration in weight % derived from EDS analyses. Number of measurements in brackets

Table 4: Modelled trace element composition of different thin section domains. The composition was calculated using the modal content from Table 2 and multiplied by the average trace element concentration of each accessory mineral in Table 3. The data is compared to the ranges of whole rock compositions in Fig. 13. A more detailed table, including the contributions of single minerals is provided in Electronic Appendix 5.

	Zr [ppm]	∑LREE [ppm]	∑HREE [ppm]	Th [ppm]	U [ppm]	Y [ppm]
6ML1_1						
Leucosome	14.10	15.96	0.47	1.80	0.54	1.73
Selvedge	355.51	188.24	5.71	21.50	6.93	27.42
Mesosome	81.37	76.13	1.45	8.61	2.51	6.30
Bulk sample	82.04	60.49	1.49	6.86	2.09	6.65
6ML1_6						
Leucosome	49.09	17.26	0.56	9.23	3.54	10.99
Selvedge	108.44	23.24	0.95	12.38	4.82	15.38
Mesosome	86.51	21.26	1.24	10.97	4.15	11.53
Bulk sample	83.61	20.90	1.08	10.89	4.15	12.02
6ML21_1						
Diatexite	94.18	23.03	1.32	14.09	3.15	10.35

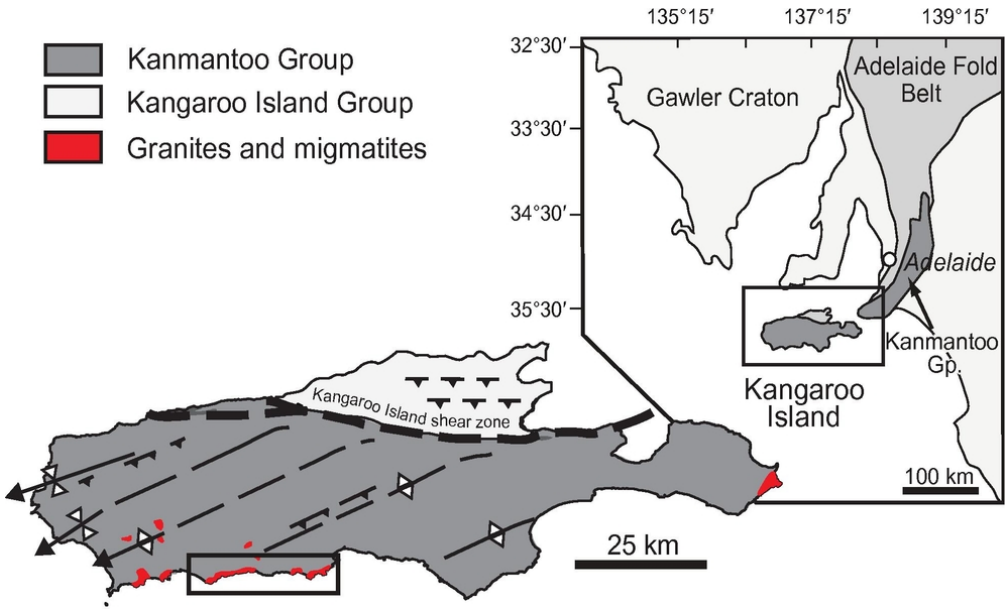

83x50mm (300 x 300 DPI)

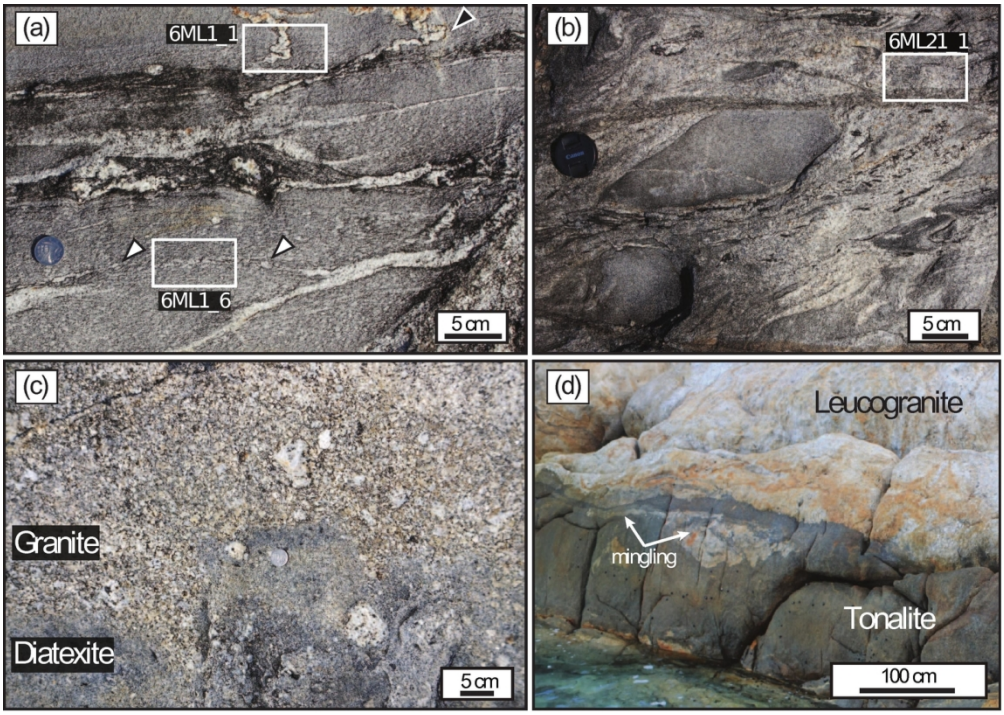

135x95mm (300 x 300 DPI)

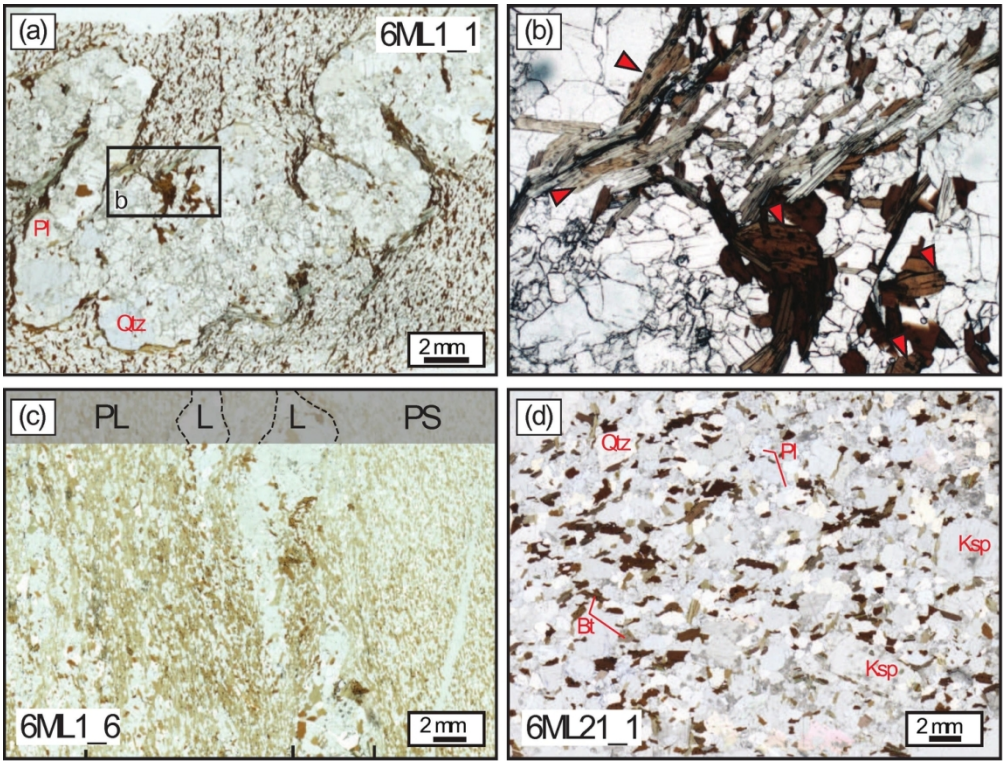

127x96mm (300 x 300 DPI)

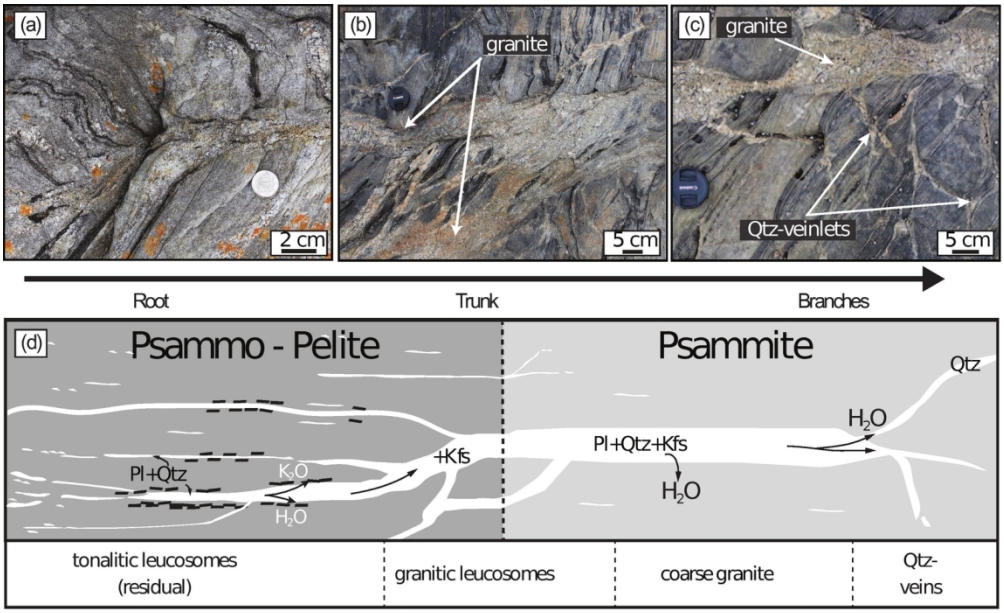

138x84mm (300 x 300 DPI)

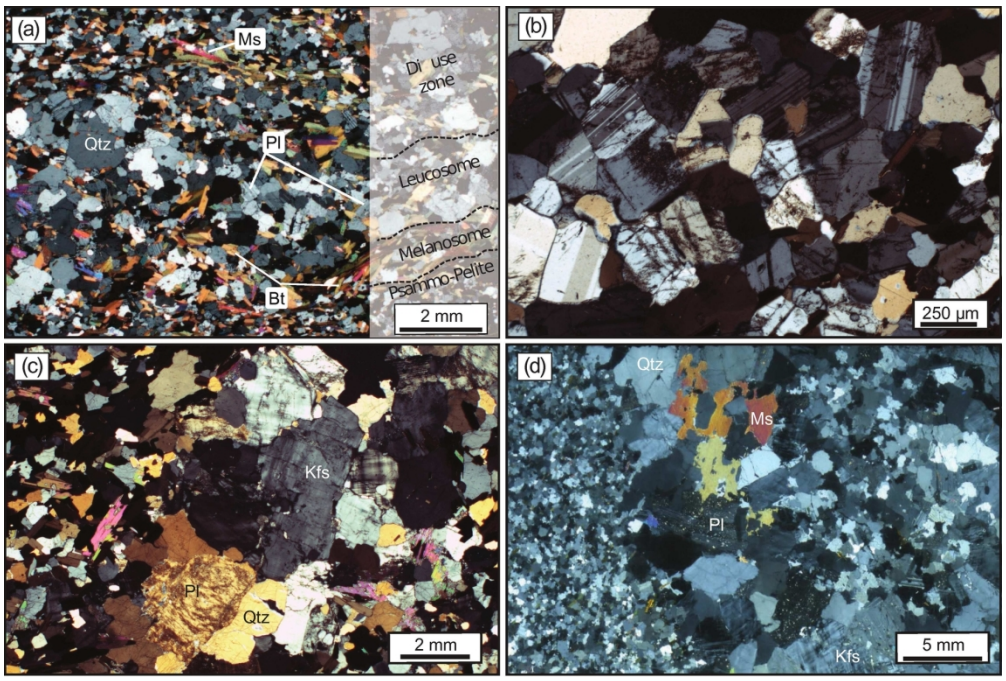

163x109mm (300 x 300 DPI)

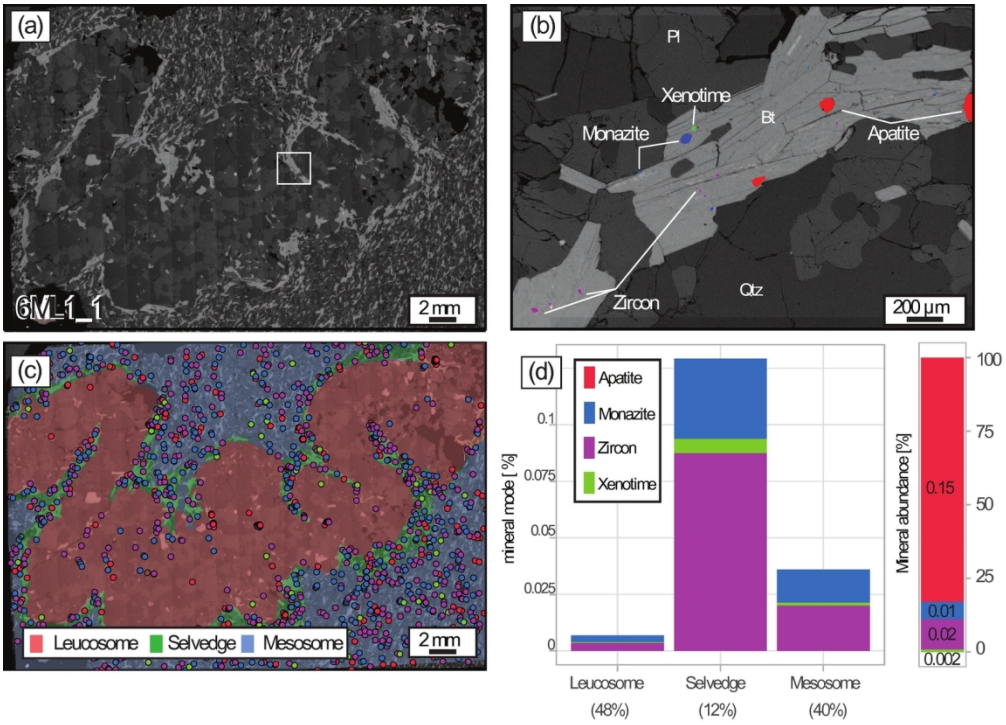

142x102mm (300 x 300 DPI)

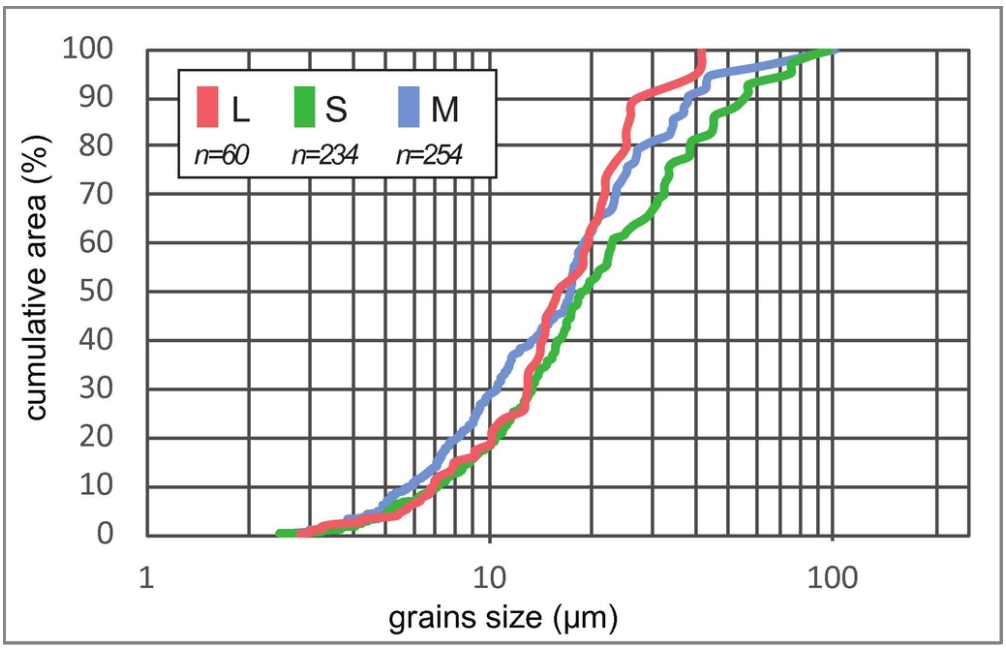

87x56mm (300 x 300 DPI)

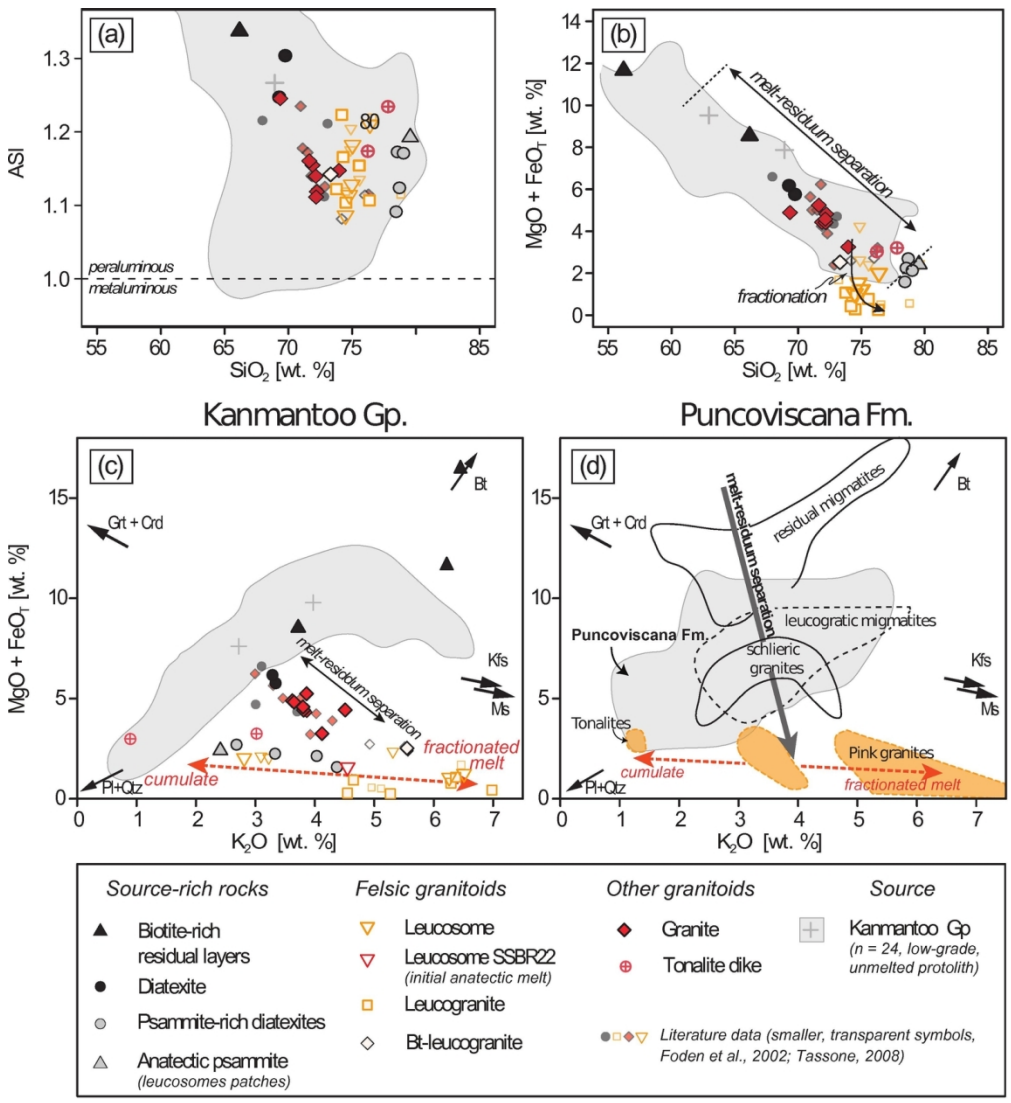

134x146mm (300 x 300 DPI)

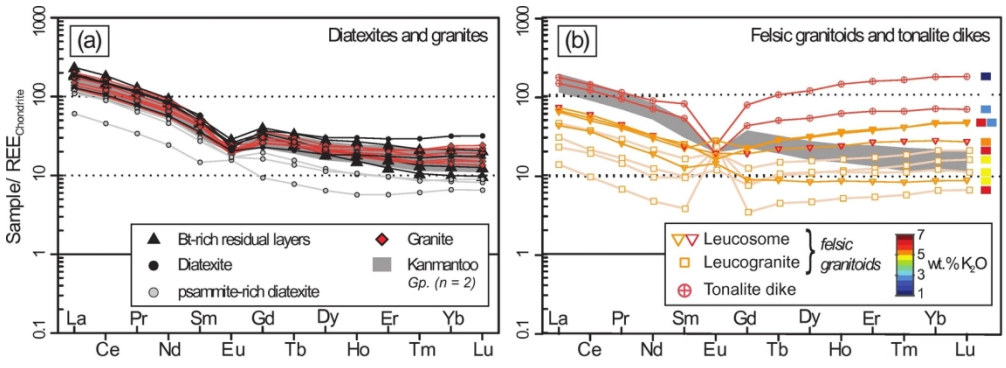

147x51mm (300 x 300 DPI)

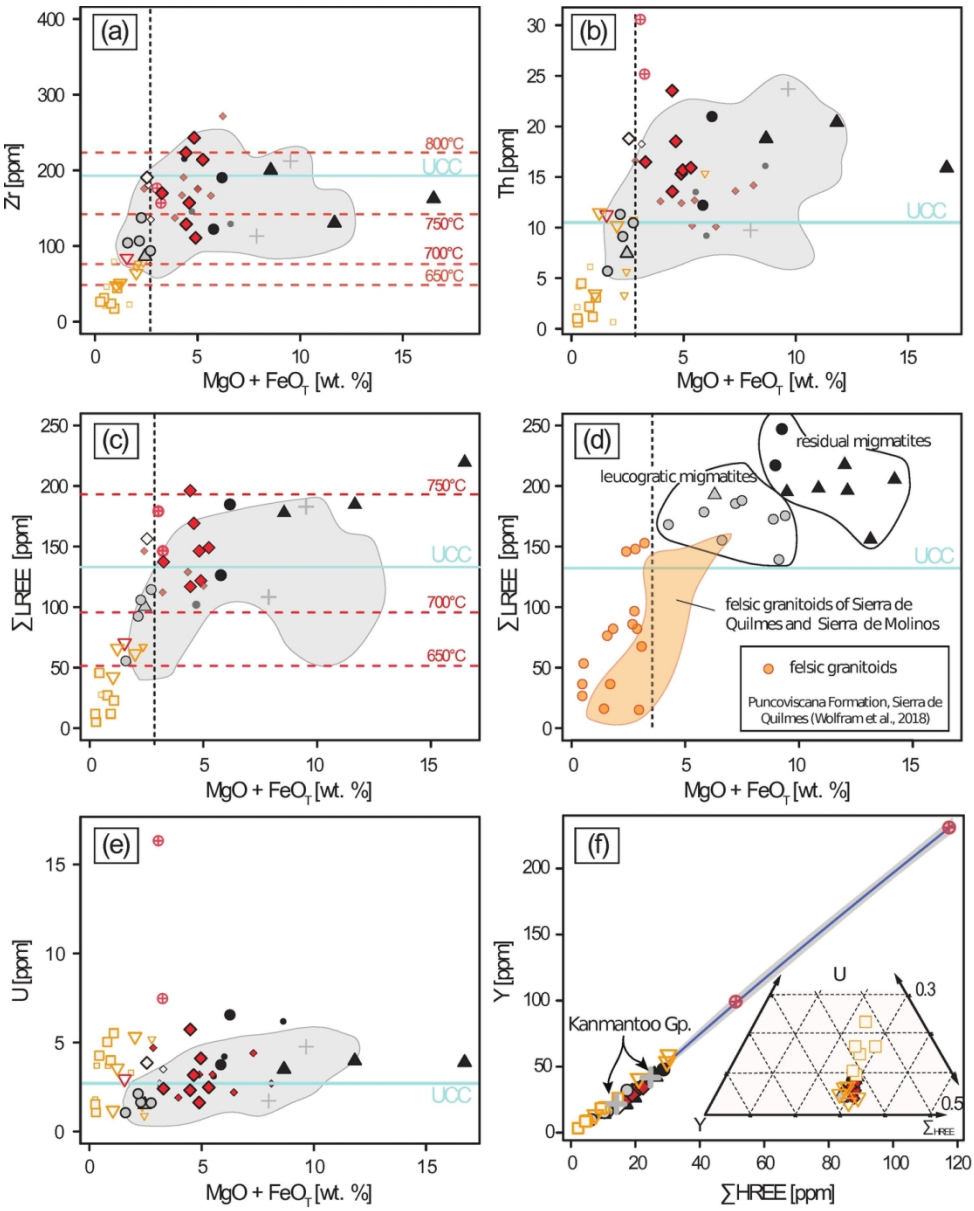

125x155mm (300 x 300 DPI)

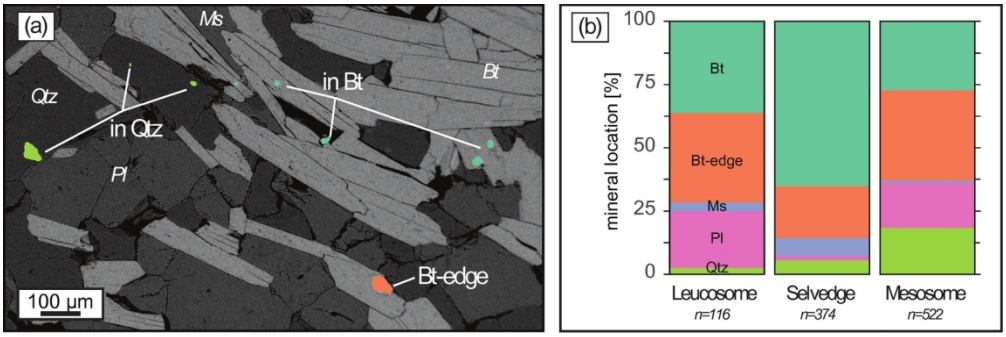

155x51mm (300 x 300 DPI)

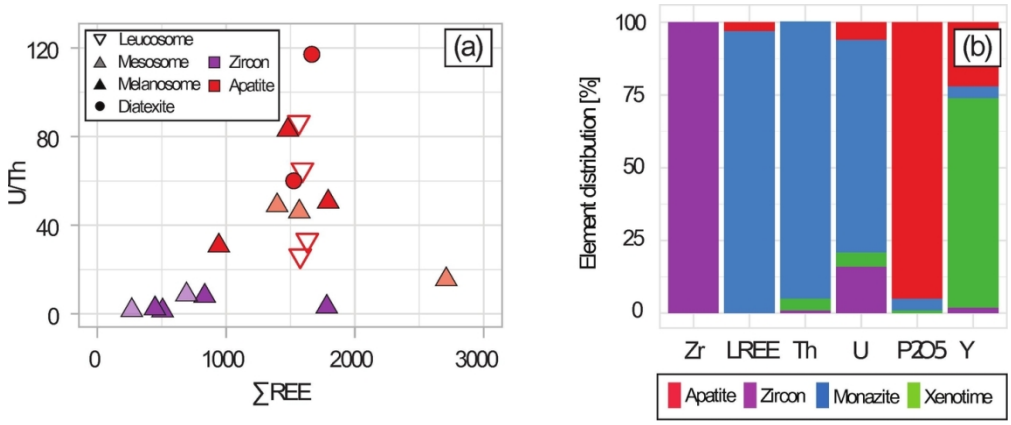

122x50mm (300 x 300 DPI)

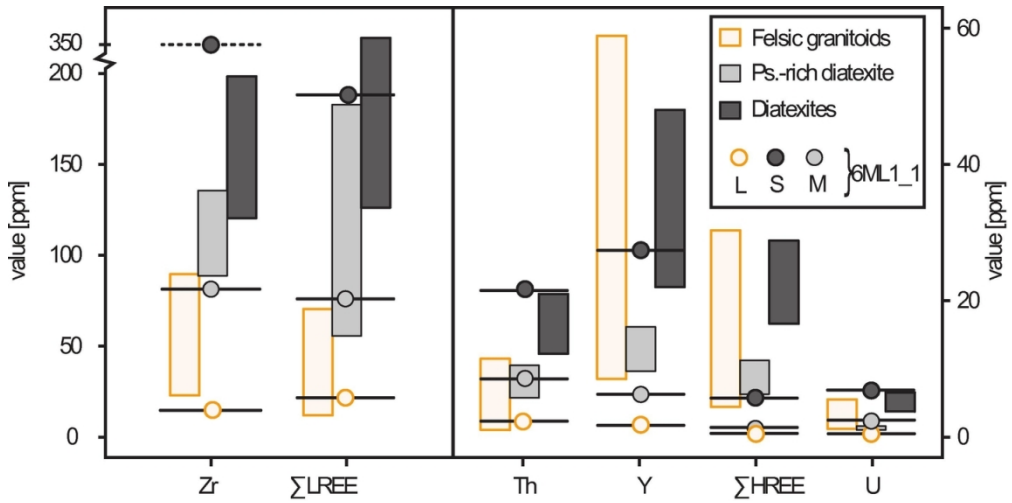

120x59mm (300 x 300 DPI)

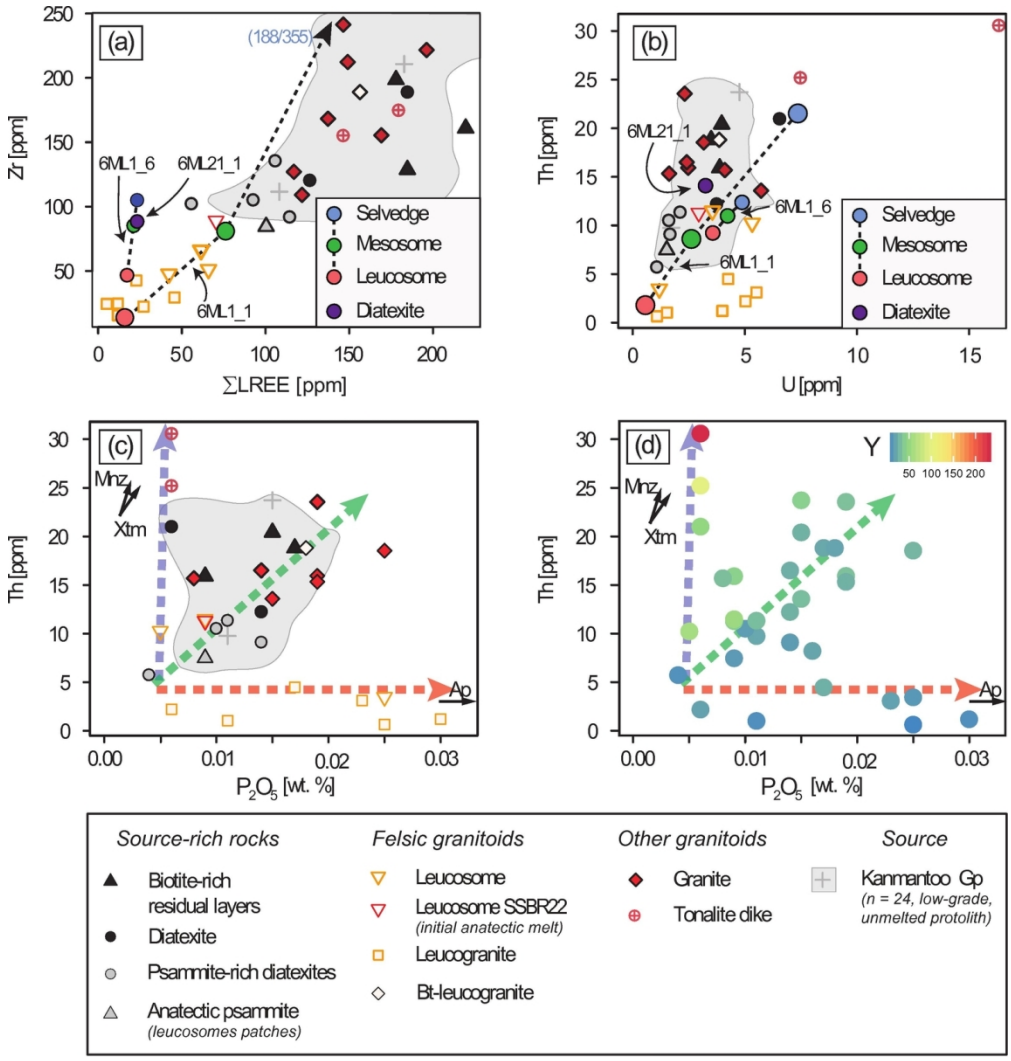

134x141mm (300 x 300 DPI)